Annual Review of Earth and Planetary Sciences

Elastic Thermobarometry

Matthew J. Kohn,[1] Mattia L. Mazzucchelli,[2] and Matteo Alvaro[3]

[1]Department of Geosciences, Boise State University, Boise, Idaho, USA; email: mattkohn@boisestate.edu

[2]Mainz Institute of Multiscale Modeling and Institute of Geosciences, Johannes-Gutenberg University of Mainz, Mainz, Germany

[3]Department of Earth and Environmental Sciences, University of Pavia, Pavia, Italy

Annu. Rev. Earth Planet. Sci. 2023. 51:331–66

The *Annual Review of Earth and Planetary Sciences* is online at earth.annualreviews.org

https://doi.org/10.1146/annurev-earth-031621-112720

Keywords

metamorphism, pressure-temperature, Raman spectroscopy, elastic, viscous, plastic

Abstract

Upon exhumation and cooling, contrasting compressibilities and thermal expansivities induce differential strains (volume mismatches) between a host crystal and its inclusions. These strains can be quantified in situ using Raman spectroscopy or X-ray diffraction. Knowing equations of state and elastic properties of minerals, elastic thermobarometry inverts measured strains to calculate the pressure-temperature conditions under which the stress state was uniform in the host and inclusion. These are commonly interpreted to represent the conditions of inclusion entrapment. Modeling and experiments quantify corrections for inclusion shape, proximity to surfaces, and (most importantly) crystal-axis anisotropy, and they permit accurate application of the more common elastic thermobarometers. New research is exploring the conditions of crystal growth, reaction overstepping, and the magnitudes of differential stresses, as well as inelastic resetting of inclusion and host strain, and potential new thermobarometers for lower-symmetry minerals.

- A physics-based method is revolutionizing calculations of metamorphic pressures and temperatures.
- Inclusion shape, crystal anisotropy, and proximity to boundaries affect calculations but can be corrected for.
- New results are leading petrologists to reconsider pressure-temperature conditions, differential stresses, and thermodynamic equilibrium.

INTRODUCTION

We do not know when humans first began to care about inclusions of one mineral inside another, but it must have been long ago because middle Paleolithic (c. 50–300 ka) humans were preferentially selecting inclusion-free quartz crystals to fabricate stone tools (e.g., see Wurz 2013, and references therein; see also Reher and Frison 1991). With the dawn of modern science, Pliny the Elder (1855) reported mineral inclusions in his *Natural History* (c. 77 AD), whereas Steno (1669) first interpreted inclusions to represent crystals that formed either before or during crystallization of the host phase. By the 1800s, fractures and unusual optical black crosses were reported around inclusions in diamond and a few other minerals and correctly interpreted to reflect local differential stresses between inclusion and host (Brewster 1820, Sorby & Butler 1869) (**Figure 1**). Sorby & Butler's (1869) sesquicentennial interpretation forms the basis of elastic thermobarometry. Conceptually, when a host crystal entraps an inclusion, there is no differential stress or strain (the volume of the inclusion exactly matches the volume of the void space or hole in the host). However, as pressure-temperature (P-T) conditions change, e.g., during exhumation, the volumes of host and inclusion change differently because they have different thermal expansivities and compressibilities. These differential volume changes cause either compressive or tensile stresses.

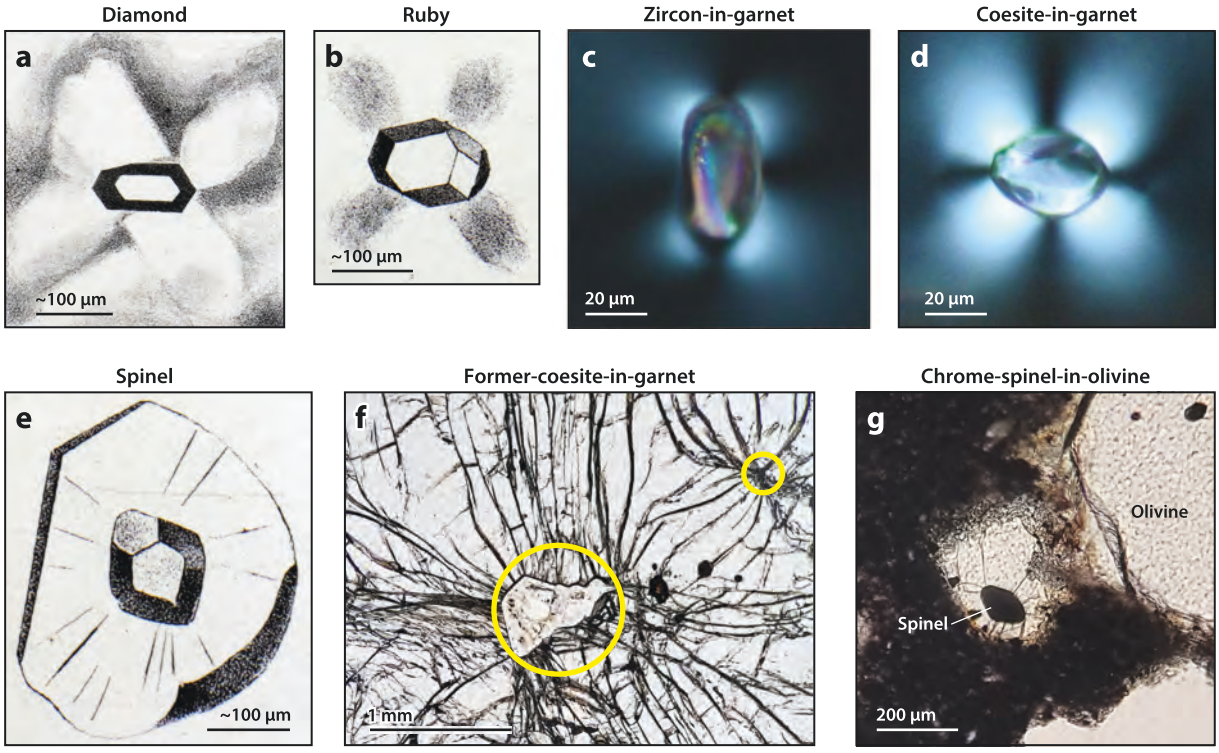

Figure 1

Evidence for development of stress between inclusions and host crystals, from either birefringent haloes (elastic strain) or fractures (plastic strain). (*a*,*b*) Sketches of birefringent haloes around inclusions (unidentified) in diamond and ruby (Sorby & Butler 1869). (*c*,*d*) Photomicrographs of birefringent haloes in garnet around zircon and coesite (Campomenosi et al. 2018). (*e*) Sketch of fractures in spinel around solid inclusion (Sorby & Butler 1869). (*f*) Photomicrograph of fractures in garnet around former coesite (*yellow circles*). (*g*) Photomicrograph of fractures in olivine around chrome-spinel. Panels *a*, *b*, and *e* reproduced with permission from Sorby & Butler (1869).

Quantification of these local stresses allows calculation of entrapment P-T conditions, giving rise to the field of elastic thermobarometry.

Elastic thermobarometry differs fundamentally from conventional thermobarometry. Although both methods seek to interpret P-T conditions of mineral formation, conventional thermobarometry relies on thermodynamic inversion of chemical compositions of minerals. In contrast, elastic thermobarometry relies on elastic inversion of the physical properties of minerals. That is, conventional thermobarometry is based on chemical measurements; elastic thermobarometry is based on physical measurements.

How does elastic thermobarometry work? At its heart lies each mineral's elastic properties and its equation of state (EoS) (P-T dependence of its volume) (see the sidebar titled Elastic Thermobarometry Terms). Rosenfeld & Chase (1961) recognized that, because two minerals have different thermal expansivities and compressibilities, local stresses around an inclusion could be eliminated by subjecting the host-inclusion system to elevated P or T (**Figure 2**). That is, for the excess stress on an inclusion today, there is some other P-T condition at which the mismatch in volume between the inclusion and the hole in the host crystal exactly disappears. This would eliminate the differential compressive or tensile stress between the inclusion and surrounding host. In fact, because volumes depend on both pressure and temperature, a line in P-T space satisfies this condition (**Figure 2**). If the host crystal has not relaxed or fractured around the inclusion, the P-T condition of inclusion entrapment must occur somewhere along this line. Various terms have been used for the lines, including null curve (Rosenfeld & Chase 1961), zero volume difference (Izraeli et al. 1999), or isovolume locus (Barron 2003), but most researchers now use the term isomeke [Greek for equal length (Adams et al. 1975)]. Different mineral inclusions in the same host crystal will have different orientations and spacings of isomekes [e.g., quartz-in-garnet (QuiG) and zircon-in-garnet (ZiG)] (**Figure 2**). In principle, the intersection of isomekes for different inclusions from the same portion of a crystal can yield the P-T conditions of entrapment (**Figure 2**), while inclusions in different parts of a crystal can yield a P-T path.

This simple concept of isomekes and elastic thermobarometry receives significant experimental and empirical support, but recent research also reveals numerous complications. Local stresses can be affected by inclusion shape, proximity to other inclusions or surfaces, anisotropic expansivities and compressibilities (for noncubic crystals), and inelastic processes. In this review, we first describe how stresses are determined and develop the basic theory. We then discuss theoretical refinements to account for geometry, anisotropy, and inelastic processes that can reset stresses. Finally, after presenting examples, we offer thoughts on future research.

HOW DO WE DETERMINE STRESS?

Stress cannot be measured directly; rather, we measure strain and, knowing the elastic properties of minerals, calculate stress. Strain falls into three categories: elastic, viscous, and plastic. Elastic strain is completely recoverable and is the basis for elastic thermobarometry. For example, if an inclusion with only elastic strain is removed from its host, it will recover its standard-state (1 bar, 298 K) volume and will not retain any permanent strain. Viscous and plastic deformations are permanent strains. Viscous strain occurs continuously and reflects the relaxation of a crystal to stress gradients. Viscous strain rate depends exponentially on temperature. If temperature is high enough, any differential stress between host and inclusion causes the host crystal to relax, relieving the stress. In that case, the original entrapment P-T condition is not recoverable. However, during cooling, the host crystal transitions from dominantly viscous behavior to dominantly elastic. Below the temperature at which that occurs—the host mineral's mechanical closure temperature—differential stresses can build up. In that case, elastic thermobarometry allows calculation of a closure isomeke, rather than an entrapment isomeke. Plastic strain is a threshold

ELASTIC THERMOBAROMETRY TERMS

α: thermal expansivity
β: compressibility
Elastic relaxation: (*a*) the theoretical elastic response of an inclusion and host in response to a pressure step (Angel et al. 2014b, 2017b) and also called elastic interaction; (*b*) the relaxation of elastic strain due to viscous response in the host (Moulas et al. 2020)
EntraPT: online software that converts strains to P_{inc} and P_{inc} to isomekes (Mazzucchelli et al. 2021); duplicates some functionality of EosFitPinc
EosFitPinc: standalone software that calculates isomekes and P_{inc} using equations of state for host and inclusion (Angel et al. 2017b)
Equation of state (EoS): the functional dependence of a mineral's molar volume on pressure and temperature, expressed in terms of thermal expansivity (α) and compressibility (β); can be expressed either volumetrically (volume EoS) or along crystallographic axes (axial EoS)
G, G_{host}: shear modulus of the host
Grüneisen tensor: tensor that relates Raman peak shifts to strains
Host: a crystal that contains inclusions of other minerals
Inclusion: a crystal of one mineral enclosed (entrapped) inside another mineral
Isomeke: a line through P-T space for which any fractional change in volume of an inclusion exactly matches the fractional change in the void space in the host; no differential pressure occurs between the host and inclusion along the isomeke; the isomeke for an inclusion-host pair is commonly interpreted to constrain P-T conditions of entrapment, although it can represent a mechanical closure isomeke
K: bulk modulus ($= 1/\beta$)
Mechanical closure temperature: the temperature at which a host crystal transitions from viscous to elastic response to stress
P_{foot}: the stress (pressure) of the entrapment isomeke at standard-state temperature; can be either positive (compressive stress) or negative (tensile stress)
P_{host}: the external pressure on the host; at standard measurement conditions, it is 1 bar
P_{inc}: the stress (pressure) on an inclusion; can be either positive (compressive stress) or negative (tensile stress)
P_{ref}, T_{ref}: reference pressure and temperature
P_{trap}, T_{trap}: the pressure and temperature at which an inclusion was entrapped in a host
QuiG, QuiZ, ZiG, etc.: acronyms for quartz-in-garnet, quartz-in-zircon, zircon-in-garnet, etc.
Reference conditions (P_{ref}, T_{ref}): whatever P-T conditions measurements are made; most measurements are made at standard state, although slight variations in laboratory temperature are possible, and in some studies measurements are made at elevated P or T
Residual stress, residual strain: the stress or strain on an inclusion after the rock is exhumed; P_{inc} is the negative of the mean of the normal components of the residual stress
standard state: 1 bar and 25°C (298 K)
stRAinMAN: standalone software that calculates strains from Raman shifts and vice versa (Angel et al. 2019)

response. If stresses surpass a critical threshold, the mineral deforms permanently. Cracking represents a common form of plastic strain (**Figure 1*e*,*f***), although slip and twinning are other mechanisms. Typically, if cracks intersect an inclusion, no differential stress occurs between inclusion and host (the inclusion will reequilibrate to ambient conditions), and neither entrapment nor closure P-T conditions are recoverable. Raman spectroscopy, X-ray diffraction, and electron backscatter diffraction record different characteristics of strain that are relevant to interpretations.

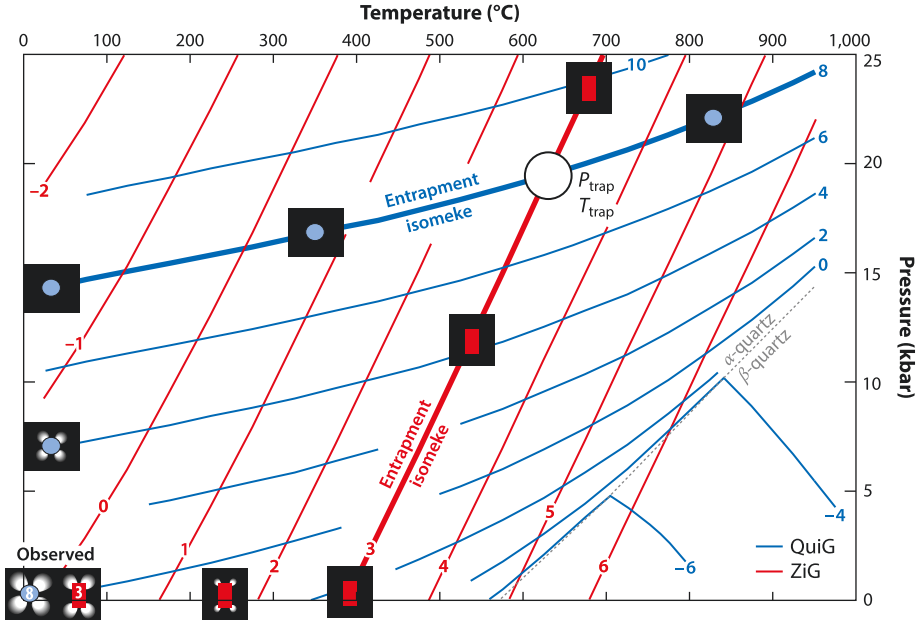

Figure 2

Pressure versus temperature diagram, contoured with isomekes for quartz-in-garnet (QuiG) and zircon-in-garnet (ZiG) to illustrate the concept of elastic thermobarometry. Contour numbers represent the pressure in kilobar that would be measured at standard state (1 bar, 298 K) for an inclusion that was entrapped along the isomeke (negative values indicate tensile stresses). For example, a garnet might contain quartz and zircon inclusions with compressive stresses of 8 and 3 kbar, respectively (schematic illustrations of birefringent haloes at room P-T; compare with **Figure 1*a–d***). Quartz is more compressible than garnet, so increasing pressure to c. 14.2 kbar (at 25°C) reduces the volume of quartz more than the volume of garnet and exactly eliminates differential stress (schematic illustration without birefringent halo). The line of zero differential stress passing through this point—the entrapment isomeke—represents possible entrapment conditions that would give rise to a quartz inclusion with compressive stress of 8 kbar. Zircon has lower thermal expansivity than garnet, so increasing temperature to c. 388°C at 1 atm increases the volume of garnet more than zircon, eliminates its differential stress, and represents one point on the zircon entrapment isomeke. The intersection of the QuiG and ZiG entrapment isomekes yields the entrapment P-T condition (P_{trap}, T_{trap}). Isomeke calculations are based on equations of state for almandine garnet (Angel et al. 2022b), quartz (Angel et al. 2017a), and zircon (Holland Powell 2011), and assume simplified spherical geometry, endmember compositions, and no elastic anisotropy.

Raman Spectroscopy

For several key reasons, Raman spectroscopy is the most common technique used to measure elastic strain on inclusions. First, confocal laser capabilities allow spectral measurement at micrometer resolution (good for small inclusions) below the surface of the host crystal. Subsurface analysis is crucial because inclusions will release their elastic strain if exposed to a free surface, such as cracks or the top or bottom of a thin section. Second, analysis is rapid, typically tens of seconds to a couple minutes. Third, analytical errors propagate to small uncertainties in isomeke placement. Fourth, instrumentation is relatively inexpensive. Last, training time is commonly reduced because most geologists already know how to locate inclusions using petrographic microscopes.

The principles of Raman spectroscopy are covered elsewhere; for example, Chou & Wang (2017) provide an overview, and Dubessy et al. (2012) provide comprehensive treatment for the Earth sciences. Nonetheless, some practical concepts provide context for later discussion. Raman

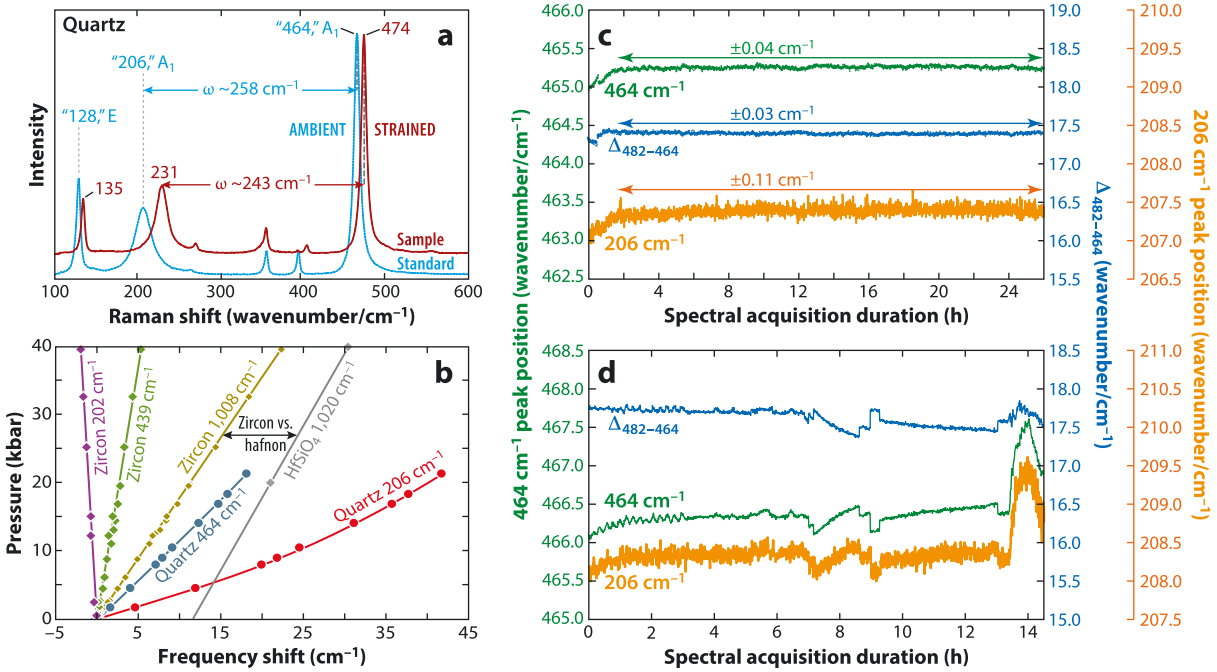

Figure 3

(*a*) Raman spectra for quartz at standard temperature and pressure (standard) and for a quartz inclusion in eclogitic garnet (sample) modified from Endo et al. (2012). The increases in peak positions and decrease in spacing between 464 and 206 peaks ($\Delta\omega$) indicate the inclusion is under compression. A_1 and E refer to types of motions among atoms. In quartz, these represent symmetric stretching and symmetric bending, respectively, in the SiO_4 subunit. (*b*) Correlation between pressure and peak position, showing different sensitivities for different vibrational frequencies (quartz and zircon) and effect of composition on peak position (zircon versus hafnon; *double arrow*). Data are from Knittle & Williams (1993), Hoskin & Rodgers (1996), and Schmidt et al. (2013). (*c*,*d*) Peak position reproducibilities for quartz at standard temperature and pressure (Cizina et al. 2023), showing good reproducibility for stable laboratory conditions (*c*) but abrupt shifts in peak positions for less controlled laboratory conditions (*d*). If a 532-nm laser source is used, shifts can be monitored and partially corrected by simultaneous measurement of an artificial ~484-cm^{-1} Hg-emission line introduced with a fluorescent lamp. Minimum analytical reproducibility propagates to uncertainties in P (at assumed T) of less than 50 bars, comparable to propagated analytical uncertainties arising from chemical measurements and conventional thermobarometry (Kohn & Spear 1991).

spectroscopy samples vibrational frequencies, and spectra are reported in frequency units of cm^{-1} (= waves/cm) (**Figure 3**). Each mineral possesses characteristic frequencies that correspond to fundamental vibrations of bonded atoms in the crystal (**Figure 3*a***). For example, the A_1 mode in quartz corresponds with symmetric stretching of the SiO_4 subunit (expansion and contraction of oxygen atoms around a central Si; peaks at ~206 and 464 cm^{-1}), whereas the E mode corresponds with symmetric bending (peak at ~128 cm^{-1}). Frequencies vary depending on bonding state (crystal structure), strain (bond length and angle, which depend on temperature and stress), and composition. Thus, spectra will differ depending on crystal structure (e.g., quartz versus coesite), strain state [e.g., compressed versus expanded quartz (**Figure 3*a*,*b***)], or chemical composition [e.g., zircon versus hafnon (**Figure 3*b***)]. Elastic thermobarometry typically ignores signal intensities because they depend on numerous factors, including the laser frequency, depth of inclusion below the surface, transparency/absorption of the host (which depends on mineralogy and chemical composition), orientation of the inclusion (if it is structurally anisotropic), and fluorescence.

Under homogeneous compression, bonds normally shorten, frequencies increase, and Raman peak positions shift upward (**Figure 3*a*,*b***). Under expansion, the reverse occurs. Thus,

simplistically, the magnitude of the upward or downward shift in peak positions, relative to a standard-state (1 bar, 298 K) measurement of the same material, must correlate with strain that in turn correlates with stress (**Figure 3*b***). Recognizing this, Parkinson & Katayama (1999), Parkinson (2000), and Sobolev et al. (2000) first used the position of the characteristic ∼521-cm^{-1} Raman peak for coesite inclusions inside garnet and diamond to calculate in situ pressures. Because different peaks for a mineral can show different pressure sensitivities, the differential shift between peaks (widening versus narrowing) has also been proposed as a stress sensor (Enami et al. 2007). The latter approach is less sensitive to instrument drift or calibration of a reference spectrum. Although some instrumentation in a controlled laboratory environment (e.g., temperature, humidity, voltage, etc.) can be extremely stable over long analytical sessions [c. ±0.03 cm^{-1} (**Figure 3*c***)], conferring high precision in inferred isomeke position (<±50 bars), less well-controlled laboratory conditions can lead to abrupt shifts in peak positions [c. 1 cm^{-1} (**Figure 3*d***)] and larger errors [±1 kbar (Cizina et al. 2023)].

Single- or paired-peak calculations of stress are fully accurate only for spherical, isotropic inclusions inside isotropic hosts, a condition that few mineral systems approximate outside of garnet, spinel (group), and diamond. The ubiquity of anisotropic systems, especially nonspherical inclusions of quartz (hexagonal crystal system) and zircon (tetragonal crystal system) in other minerals, has prompted research on the effects of other geometries and on noncubic crystal-system inclusions and hosts. Very generally, the simple correspondence between Raman peak position and pressure (**Figure 3*b***) breaks down for these systems and can require more complicated inversion of the stiffness tensor of the mineral to recover crystal-axis-specific strains. In practice, this is accomplished by using density functional theory (DFT) to calculate a Grüneisen tensor (Murri et al. 2018, Angel et al. 2019, Stangarone et al. 2019), which interrelates phonon mode (Raman wavenumber shift) and axis-specific strains. The programs stRAinMAN (Angel et al. 2019) and EntraPT (Mazzucchelli et al. 2021) convert Raman shifts to axial strains for common host-inclusion pairs. The axial strains are then used to determine axial stresses, which are averaged to recover average stress or pressure across an inclusion (P_{inc}). EntraPT also makes these calculations.

X-Ray Diffraction and Electron Backscattered Diffraction

Reliable, accurate, and precise Raman spectroscopy measurements on inclusions are relatively simple. A small beam size, fixed sample position, and good optics allow users to avoid complex edges, corners, clusters of inclusions, etc. (see the following discussion on system geometry). X-ray diffraction provides an alternative and complementary method to measure residual strains on inclusions (e.g., Nestola et al. 2011), but this is technically more difficult.

Initial X-ray studies were first performed on inclusions in diamond because its optical transparency and low X-ray absorbance simplified targeting inclusions and permitted relatively low radiation energies available to conventional X-ray laboratory sources (data were collected on film cameras) (Mitchell & Giardini 1953, Futergendler & Frank-Kamenetsky 1961, Harris et al. 1970). As with Raman spectroscopy, X-ray diffraction does not directly measure an inclusion's stress state; instead, the stress state is inferred from the difference between the values of the unit-cell parameters measured for the inclusion (average strains) relative to a crystal of the same material at room conditions, assuming the pressure dependencies of the unit-cell parameters for that crystal are known.

X-ray diffraction measurements are difficult for two reasons. Measurement precision represents the first hurdle. Ideally, we wish to calculate P_{inc} to within ∼10 MPa, but stiffness in crystals is typically of the order of 100 GPa. Thus, measurement of cell parameters (axial strains) requires precisions of ∼1 part in 10,000 (= 10 MPa/100 GPa). Such precise measurements can require hours for laboratory conditions, albeit only a few minutes for high-intensity sources at large-scale

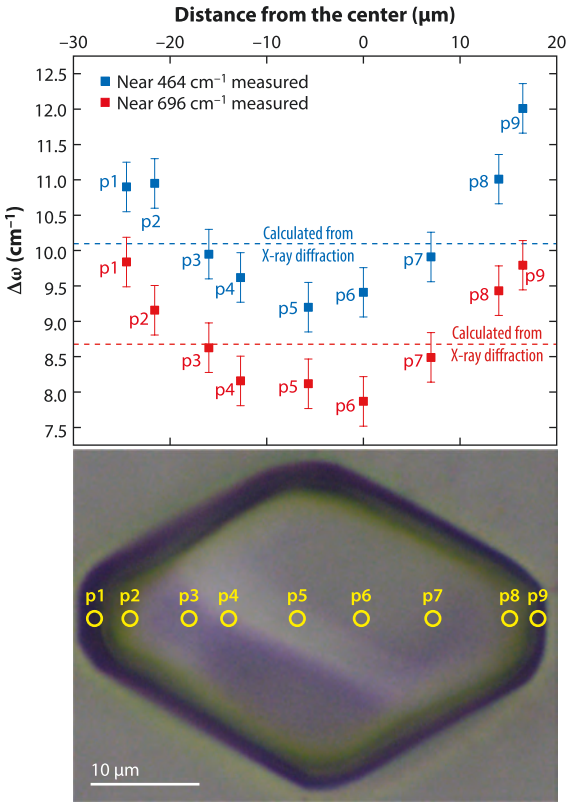

Figure 4

Wavenumber shifts ($\Delta\omega$) for the 464- and 696-cm^{-1} modes across a faceted inclusion of quartz-in-pyrope. High values indicate stress concentration near corners. X-ray diffraction allows calculation of average strain across inclusion, which can be inverted using the mode Grüneisen tensor to calculate the average shift (*dashed lines*). Figure adapted with permission from Murri et al. (2018).

facilities. Sample centering represents a second significant hurdle. X-ray diffraction measurements require sample rotation during data collection, and to maintain focus, the inclusion must be positioned within a few microns of the goniometer center (center of rotation of all the diffractometer axes). Even in the early 1950s scientists recognized that centering the inclusion represented a large source of error, and special protocols are necessary (Angel et al. 1997, 2022a).

Because X-ray beams are typically more than 100 μm wide, most single-spot analyses encompass the entire inclusion (and a significant portion of the host) and determine an average strain (Murri et al. 2018, Angel et al. 2022a). Although strain is homogeneous for a spherical inclusion (Eshelby 1957), irrespective of the symmetry of the host or inclusion crystals, stresses and strains concentrate at edges and corners of faceted inclusions. Consequently, whereas Raman measurements can reveal strain gradients across a shaped inclusion (e.g., Enami et al. 2007; Zhukov & Korsakov 2015, Campomenosi et al. 2018, Murri et al. 2018), X-ray measurements show an average strain (**Figure 4**). In general, for complex geometries both X-ray and Raman measurements should be preferred in combination with numerical simulation on the exact shape of the inclusion (e.g., Mazzucchelli et al. 2018). X-ray diffraction also provides precise crystallographic orientations of inclusion and host, which are important when working with elastically anisotropic mineral pairs (Gonzalez et al. 2021). Calculated orientations are not sensitive to small offsets of the crystal from

the center of the diffractometer (Nimis et al. 2019). Relative peak intensities in Raman spectra can also indicate crystal orientation (Hopkins & Farrow 1986; Zhong et al. 2021b), but uncertainties are much larger than for X-ray measurements.

High angular resolution electron backscatter diffraction can be used to map crystallographic texture, grain orientation, grain shape, and local strain across an exposed polished surface (e.g., Wallis et al. 2019). Using crystal-axis-specific stiffness coefficients, strain maps can be inverted to infer distributions of stress, which are rarely uniform across crystals (Wallis et al. 2019). Because electrons penetrate only 1–2 μm for typical accelerating voltages, analysis is essentially limited to surfaces, and investigation of buried inclusions is not possible. However, measurement across partially exposed inclusions can determine their orientation with respect to their hosts, distinguish types of strain, and quantify densities of geometrically necessary dislocations (Wallis et al. 2019).

FOUNDATIONAL MODEL: PURELY ELASTIC, SPHERICAL, AND ISOTROPIC

As will be seen, elastic thermobarometry relies on quantitative modeling of P_{inc}, but qualitatively, what determines its magnitude? In an elastic system, the residual pressure of the inclusion is controlled primarily by the contrast in how the host and inclusion respond to stress and temperature. We assume that at entrapment (P_{trap}, T_{trap}) the inclusion fits perfectly within the cavity of the host and that the pressure of the inclusion (P_{inc}), the pressure of the host (P_{host}), and the external pressure (P_{trap}) are all equal. When the external pressure and the temperature change after entrapment, the two minerals will attempt to expand or shrink according to their EoSs (Rosenfeld & Chase 1961). Although compressibilities and expansivities are nearly constant, they do depend slightly on pressure and temperature, and these dependencies should be accounted for.

If an inclusion and host have identical thermoelastic properties, they will not experience any differential change to molar volumes during exhumation and cooling, and P_{inc} will not deviate from P_{host}, regardless of P_{trap}, T_{trap}. Although no two minerals have identical EoSs, some are sufficiently similar (e.g., kyanite and garnet) that P_{inc} will never be sensitive to P_{trap}, T_{trap}. Similarly, if P_{trap} and T_{trap} happen to fall along an isomeke that includes the measurement P-T conditions, measured P_{inc} must again be the same as P_{host} ($= P_{ref}$). This is because the isomeke is defined as a line along which the change in volume of the cavity (host) and of the inclusion are equal. This latter condition implies that P-T space is divided into two different domains—a region within which P_{inc} is positive (inclusion is under compression) and another within which P_{inc} is negative (inclusion is under tension).

When the host and the inclusion have different thermoelastic properties, $P_{inc} \neq P_{host}$ for all P-T conditions that do not fall along the entrapment isomeke. Whenever $P_{inc} \neq P_{host}$ (e.g., the rock follows a P-T path that deviates from the entrapment isomeke), the host and inclusion volumes change differentially, and an elastic interaction occurs between the host and the inclusion to maintain mechanical equilibrium. The magnitude of the resulting strain on the inclusion depends on how large the potential volume differences are between host and inclusion (the contrast in their EoSs), the relative compressibilities of host and inclusion (the magnitude of their elastic interaction), and the shear modulus of the host (Goodier 1933, Eshelby 1957). Large differences in compressibilities or expansivities between host and inclusion and large values of K_{host} lead to large absolute values of P_{inc}. The interaction also modifies the stress field in the system such that the radial and tangential components of the stress in the host are no longer equal (**Figure 5**).

Goodier (1933) and Eshelby (1957) laid the foundation of the analytical description of the elastic interaction, which begins with a simple model of a spherical, isotropic inclusion entrapped inside an infinite isotropic host (see also Mura 1987). Assume the inclusion is far from any interfaces, such as cracks or crystal surfaces, and that entrapment P-T conditions were such that

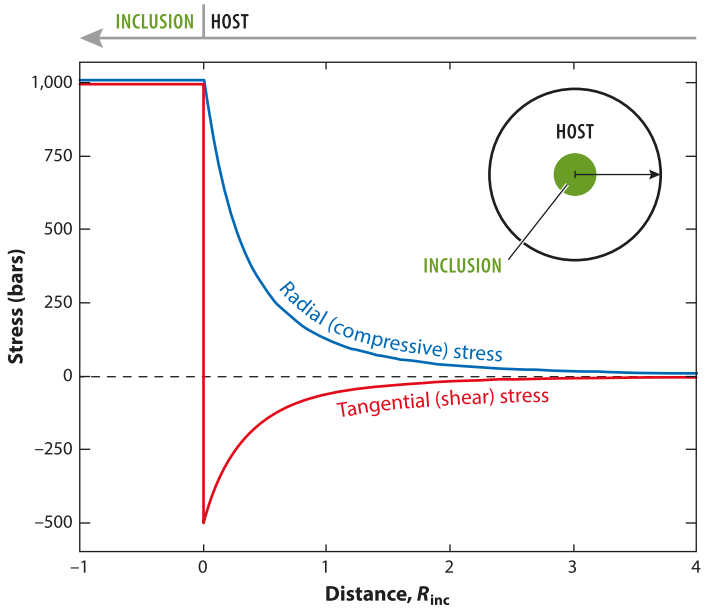

Figure 5

Stress versus distance normalized to inclusion radius, assuming $P_{inc} = 1$ kbar. Stresses in the host decrease rapidly as $1/r^3$, so that at radial distances of $\sim 3 \cdot R_{inc}$, stresses in the host are nearly zero.

the inclusion is now under compressional stress, so its volume is less than that of a free crystal at standard state. Under these conditions, the spherical (or in general ellipsoidal) inclusion has a homogeneous compressional stress and strain distribution across it (Eshelby 1957). The host experiences an identical compressional radial stress at the interface with the inclusion, but its external surface is at standard state. Consequently, stress and strain must decrease outward from the inclusion. Several studies have derived the stress distribution in a spherical host around a centered spherical inclusion (e.g., Eshelby 1957, Tait 1992, Zhang 1998, Bower 2010) (**Figure 5**) (here compressive stress is taken as positive):

$$\sigma_{radial} = \frac{(P_{inc} - P_{host}) \cdot R_{host}^3 \cdot R_{inc}^3}{(R_{host}^3 - R_{inc}^3) \cdot r^3} - \frac{P_{inc} \cdot R_{inc}^3 - P_{host} \cdot R_{host}^3}{R_{host}^3 - R_{inc}^3}, \quad 1a.$$

where P_{inc} is inclusion pressure, P_{host} is host pressure, R_{inc} is inclusion radius, and R_{host} is host radius. The tangential stress distribution (here negative; radial compression induces tangential extension in two orthogonal directions) (**Figure 5**) is

$$\sigma_{tangential} = -\frac{(P_{inc} - P_{host}) \cdot R_{host}^3 \cdot R_{inc}^3}{2 \cdot (R_{host}^3 - R_{inc}^3) \cdot r^3} - \frac{P_{inc} \cdot R_{inc}^3 - P_{host} \cdot R_{host}^3}{R_{host}^3 - R_{inc}^3}. \quad 1b.$$

For small inclusions inside large crystals ($R_{inc} \ll R_{host}$) and for a negligible reference pressure ($P_{inc} \gg P_{host}$), these equations simplify to

$$\sigma_{radial} = \frac{P_{inc} \cdot R_{inc}^3}{r^3} \quad 2a.$$

and

$$\sigma_{tangential} = -\frac{P_{inc} \cdot R_{inc}^3}{2 \cdot r^3}. \quad 2b.$$

Because differential stress decreases as $1/r^3$ away from an inclusion, differential stresses and stress gradients become negligible at distances ~3 times the inclusion radius (**Figure 5**). This distance gives rise to the 3x rule (Kohn 2014; Mazzucchelli et al. 2018), which provides a rough guide for identifying inclusions that are sufficiently isolated to be readily modeled—their surfaces should be at least ~3 times the inclusion radius from other crystal surfaces (including the host crystal and other inclusions) and from any sample surfaces (e.g., the top or bottom of a thin section). Depending on analytical location in an inclusion and stiffness of the host, this distance can be smaller (Zhong et al. 2020b, 2021a).

The 3x rule has two important implications. First, standard thin section thicknesses of 30 μm would limit analysis to inclusions that are centered toward the middle of the section and no more than 7.5 μm in diameter. Because inclusions are commonly larger or not well-centered, most analysts make measurements on either grain mounts or polished thick sections, typically 75–100-μm thick. Second, elastic thermobarometry is not capable of providing P-T estimates for the rims of crystals. Thus, exact comparison of elastic versus conventional thermobarometry is not always possible.

Several quantitative solutions based on continuum mechanics have been suggested in the geological literature to predict the residual pressure of an isotropic inclusion after cooling and decompression of the host along an arbitrary P-T path (van der Molen & van Roermund 1986, Zhang 1998, Izraeli et al. 1999, Guiraud & Powell 2006, Angel et al. 2014b, 2017b). Some of these solutions assume linear elasticity [constant thermoelastic properties (e.g., van der Molen & van Roermund 1986, Zhang 1998)], which allows simple inversion of P_{inc} to calculate entrapment isomekes. Moulas et al. (2020) have shown that, for $P_{trap} < 20$ kbar, calculations for QuiG that assume constant elasticity are accurate to within 10%. However, the variation of elastic properties of minerals at high pressures and temperature and/or near phase transitions can lead to larger discrepancies. Therefore, other solutions have been developed to account for material nonlinearities (Guiraud & Powell 2006, Angel et al. 2014b, 2017b). Such models adopt a small strain approximation (Zhong et al. 2020a, Angel et al. 2020) and are solved with iterative methods. Because the formulations of Guiraud & Powell (2006) and Angel et al. (2017b) are based on different strain measures, they lead to different calculated entrapment pressures, although discrepancies are usually within ~1% for common host-inclusion systems (e.g., QuiG, ZiG) (Zhong et al. 2020b). Relaxing the small strain assumption leads to only small discrepancies with respect to models with small strain approximations (Moulas et al. 2020, 2021).

Elasticity is by definition reversible and path independent; therefore, all paths from the entrapment to the final conditions should give equivalent P_{inc}. In this context, the approach of Angel et al. (2014b, 2017b) provides a computationally simple and thermodynamically rigorous solution for P_{inc}, especially for complex EoSs (**Figure 6**). In the Angel et al. (2014b, 2017b) model, the path of the host-inclusion system is considered in two steps. First, the inclusion and host are cooled along the isomeke to the standard-state temperature (**Figure 6*a***). The isomeke can be calculated numerically from the EoSs of the inclusion and host and can account for any functional complexity—compressibility and thermal expansivity do not need to be constant. Specifically, the slope of the isomeke is given by (Rosenfeld & Chase 1961, Adams et al. 1975)

$$\frac{\partial P}{\partial T} = \frac{\Delta\alpha}{\Delta\beta}, \qquad 3.$$

where α is thermal expansivity and β in isothermal compressibility at the P and T of interest. Angel et al. (2014b) refer to the resulting pressure at standard-state temperature as P_{foot}. At this point, both the host and inclusion have the same pressure (**Figure 6*a*,*b***). The pressure on the host

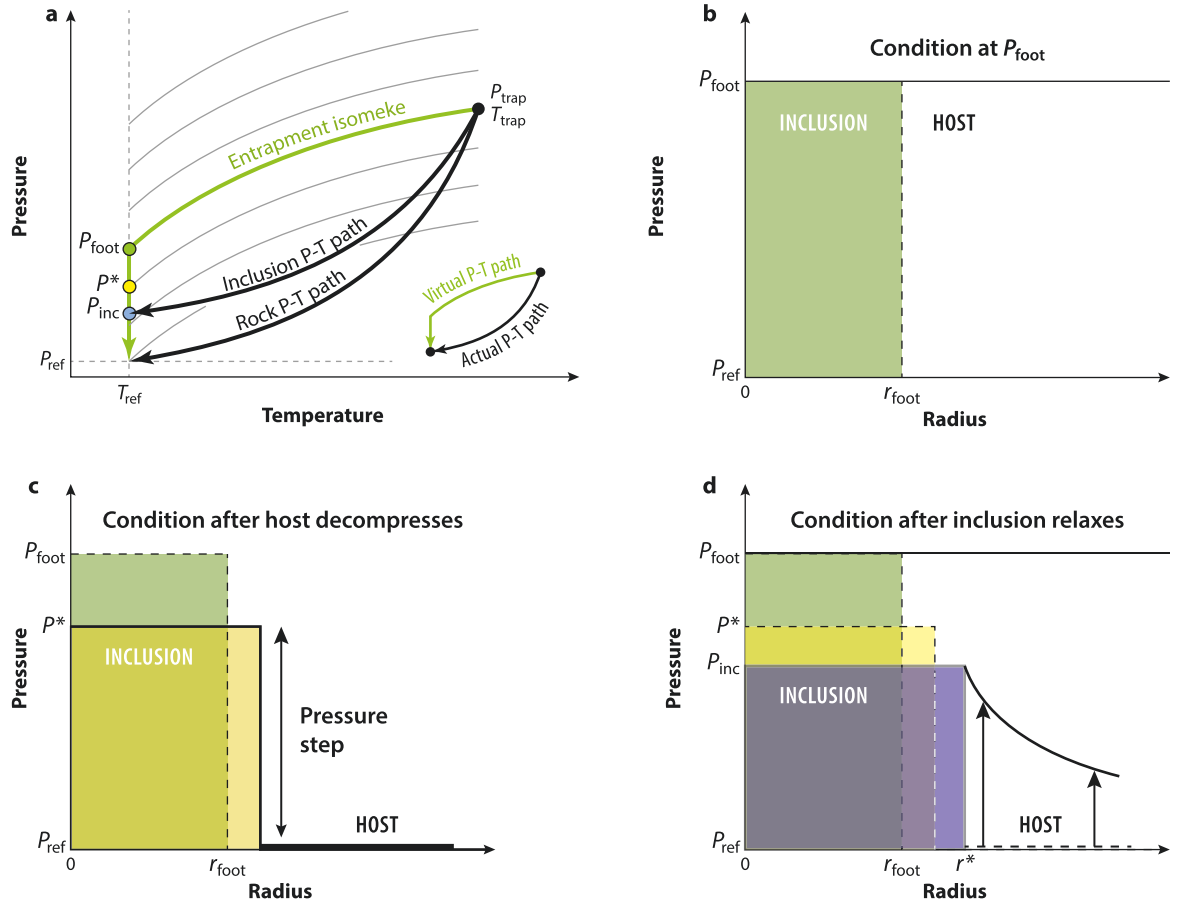

Figure 6

Concept for interrelating P_{trap}, T_{trap} and P_{inc}. (*a*) P-T diagram showing P-T paths and pressure steps in calculation. The host crystal and rock follow an actual P-T path from P_{trap}, T_{trap} to P_{ref}, T_{ref} (standard state). Inclusion follows a P-T path from P_{trap}, T_{trap} to P_{inc}, T_{ref}. The P-T path used for calculation follows the entrapment isomeke (*thick green curve*) to P_{foot}, T_{ref}. The host pressure is then reduced to P_{ref}. This causes a decrease in inclusion pressure to P^*. Stress relaxation is calculated between inclusion and host numerically to determine P_{inc}. (*b*) Condition at P_{foot}: Inclusion and host have homogeneous pressure equal to P_{foot}. Temperature is T_{ref}. (*c*) Host pressure is decreased to uniform P_{ref}. Inclusion expands and lowers pressure to P^*. (*d*) P_{inc} is calculated numerically via Equation 4, which further expands inclusion. Pressure gradient develops in host (although this is not directly calculated).

is then changed to P_{ref}, inducing a change in the volume of the host (**Figure 6*a*,*c***). For example, if $P_{foot} > 1$ (i.e., inclusion is under compression, and $P_{inc} > P_{host}$), the drop in pressure expands the hole in the host; this expansion also expands the inclusion and decreases its pressure, here denoted P^* (**Figure 6*a*,*c***). If $P_{foot} < 1$ (inclusion is under tension), the reverse is true. Because P^* differs from P_{ref}, the resulting pressure step between inclusion and host (**Figure 6*c***) will induce additional strain due to the elastic interaction[1] between the two minerals (**Figure 6*d***). The corresponding

[1] Some authors call this interaction elastic relaxation (e.g., Angel et al. 2014b, 2015, 2017b; Mazzucchelli et al. 2018, Gonzalez et al. 2021), but others use the term relaxation to describe only viscous stress release (e.g., Moulas et al. 2020).

strain can be calculated from the expression

$$\varepsilon_{inc} = \varepsilon_{host} + \frac{3(P_{inc} - P_{ref})}{4G_{host}}, \quad 4.$$

where ε is volume strain calculated relative to P_{foot} and G_{host} is the shear modulus of the host. For the host, $\varepsilon_{host} = V_{foot}/V_{ref}$, and for the inclusion $\varepsilon_{inc} = V_{foot}/V_{Pinc}$. The volume strain in the inclusion must be calculated numerically, for example iterating between assumed values of P_{inc} and ε_{inc} (Angel et al. 2017b). These calculations are commonly performed using the programs EosFit (Angel et al. 2014a), EosFitPinc (Angel et al. 2017b), or EntraPT (Mazzucchelli et al. 2021). Because volume strain is relative, Equation 4 indicates that P_{inc} is independent of inclusion size. Consequently, inclusions of a particular mineral that are entrapped at the same P_{trap}, T_{trap} must have the same P_{inc}, regardless of size (assuming they satisfy the 3x rule).

Whether a host-inclusion pair is useful for thermometry or barometry depends on how common the assemblage is, relative differences among expansivities versus compressibilities, and the shear modulus of the host. Larger differences in α and β translate into more closely spaced isomekes and greater sensitivity to either P (large $\Delta\beta$) or T (large $\Delta\alpha$). For example, quartz and many ortho-, soro-, and chain-silicates have very different compressibilities (quartz is soft), so QuiG serves as a robust barometer (Rosenfeld & Chase 1961, Adams et al. 1975, Enami et al. 2007), as do many other quartz-in-mineral equilibria, such as quartz-in-zircon (QuiZ), quartz-in-lawsonite, etc. (Kohn 2014, Cisneros & Befus 2020). Zircon and garnet have more similar compressibilities but rather different thermal expansivities, making ZiG a useful thermometer (Kohn 2014, 2016, Zhong et al. 2019a, Campomenosi et al. 2021).

Which mineral serves as host versus inclusion also affects isomekes. For example, diamond can occur as inclusions in garnet and vice versa. Slopes for both combinations are identical because the absolute differences in compressibilities and expansivities are identical (**Figure 7**). However, isomekes for diamond-in-garnet are more widely spaced, and the separation of P-T space into positive P_{inc} and negative P_{inc} is reversed (**Figure 7*a*,*b***). The spacing depends on not only the EoSs but also the shear modulus of the host (G_{host} in Equation 4). Diamond and garnet have different G_{host} (diamond is much stiffer than garnet), so isomeke spacings differ. The reversal in sign reflects the differential volume response of each mineral to pressure and temperature. Garnet has higher values of compressibility and thermal expansivity than diamond. Thus, for high P_{trap}, low T_{trap} (upper left of the P-T diagrams in **Figure 7*a***), an inclusion of garnet in diamond will attempt to expand more than the diamond host upon exhumation. Because the volume of the cavity is constrained by the diamond host, garnet will remain compressed to high P_{inc} (**Figure 7*a***). In the reverse situation (diamond-in-garnet), the garnet host (cavity) will expand more than the diamond inclusion. If the diamond inclusion remains attached to the walls of the cavity, it will be stretched and therefore under tension (negative P_{inc}) (**Figure 7*b***).

MODEL REFINEMENT 1: ACCOUNTING FOR GEOMETRY

The models above assume that the host and inclusion are elastically isotropic, and the inclusion is both spherical and located far from any boundaries. None of these conditions apply in natural systems: minerals are not elastically isotropic, inclusions are often close to grain boundaries or other inclusions, and they are not spherical. Recent numerical models have investigated how much the residual strain, stress, and pressure developed in inclusions in nonideal systems deviate from the predictions of simple models (e.g., Mazzucchelli et al. 2018, 2019; Campomenosi et al. 2018; Zhong et al. 2019b, 2021a; Morganti et al. 2020). These studies show that analytical solutions adequately describe these effects for simple cases, while numerical solutions are required for more

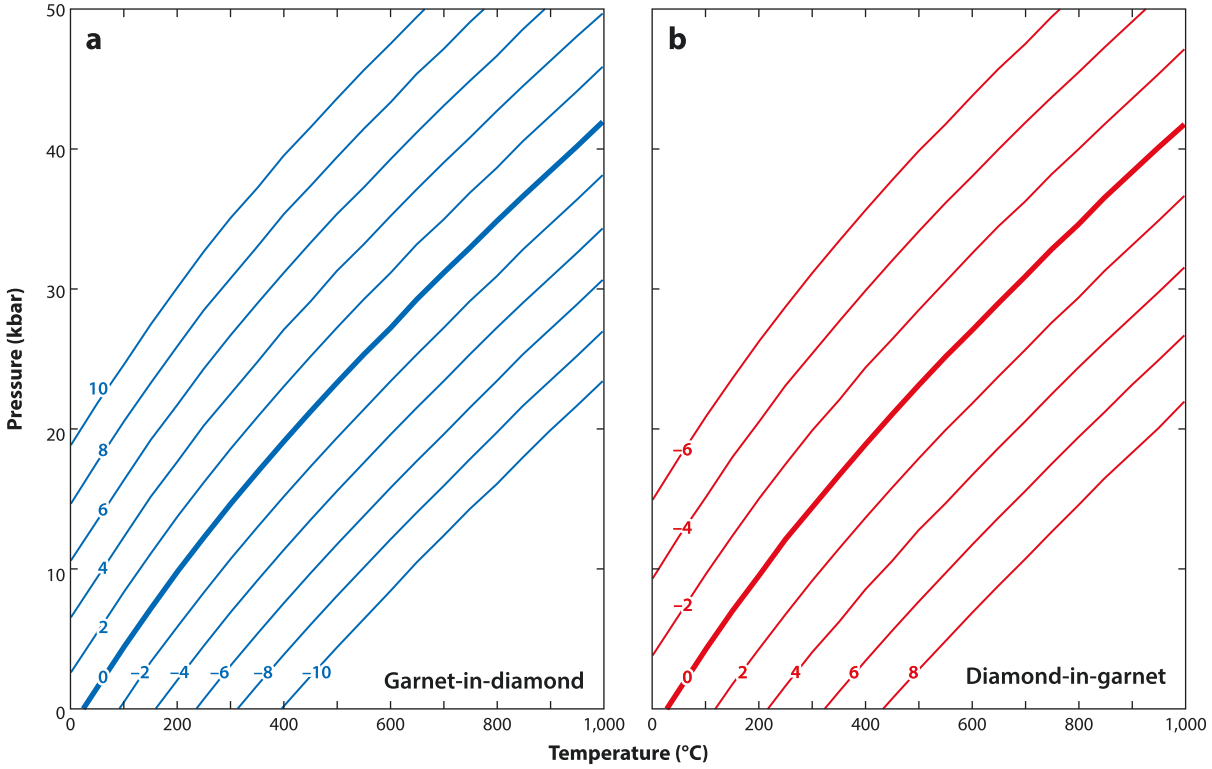

Figure 7

(*a*) Isomekes for garnet-in-diamond showing narrow spacing and positive values at higher pressure. (*b*) Isomekes for diamond-in-garnet showing wider spacing and negative values at higher pressure (the reverse of garnet-in-diamond). The slopes of the isomekes are identical (compare zero isomekes) because $\Delta\alpha$ and $\Delta\beta$ are identical at the same P-T condition but reversed in sign. Values are for P_{inc} in kbar.

complex combinations of geometries and anisotropy of elastic properties. Relatively few studies have directly measured the effect of geometry and anisotropy on the residual strain and stress (but see Murri et al. 2018, Campomenosi et al. 2018).

Inclusion Morphology

Exact analytical solutions exist for an ellipsoidal, elastically anisotropic inclusion entrapped in an infinite isotropic host (e.g., Eshelby 1957, Mura 1987, Zhong et al. 2021a). In this case, stress and strain are homogeneous across the inclusion. Fully accurate representation of faceted inclusions, anisotropic hosts, and/or more complex geometries require numerical calculations. Mazzucchelli et al. (2018) investigated how the morphology of the inclusion affects P_{inc}, assuming that both the host and the inclusion are elastically isotropic and that the host is infinite. They modeled spheroids, cylinders, and prisms with various aspect ratios to evaluate the effects of nonspherical shapes, corners, and edges. Zhong et al. (2021a) expanded models using both analytical and numerical methods to include elastically anisotropic ellipsoidal and faceted inclusions (quartz, zircon, apatite, rutile) in an infinite isotropic host (almandine). They also calculated P_{inc} for volume averages (relevant to X-ray diffraction measurements) and for centroid measurements (relevant to a single, centered Raman measurement). Results are presented in terms of the deviation of the residual pressure of each morphology compared to that of a spherical inclusion (**Figure 8**).

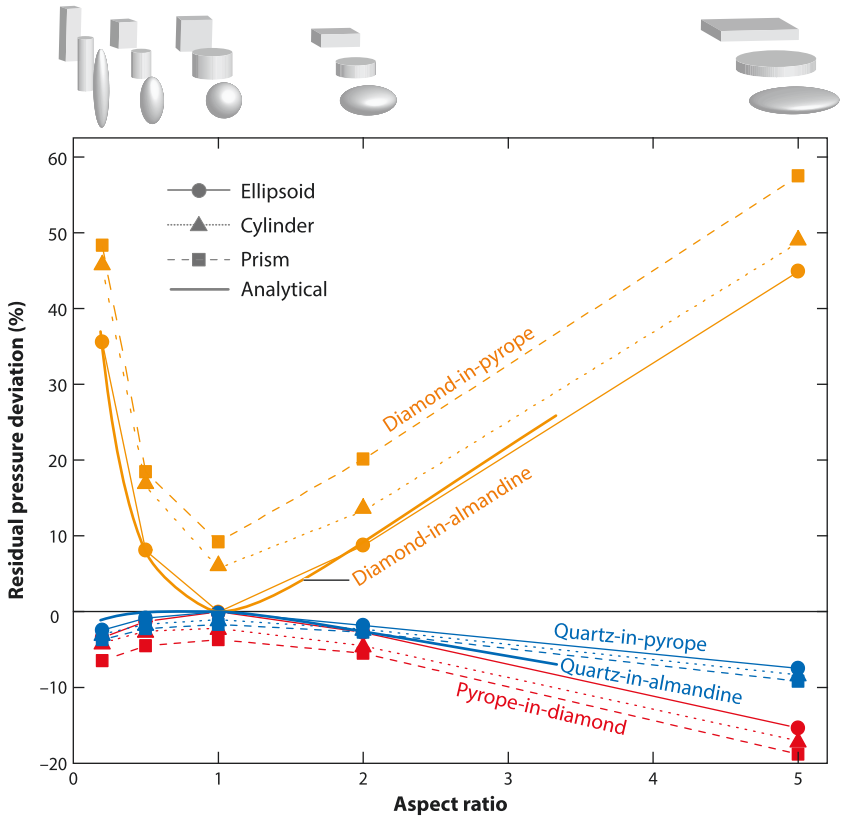

Figure 8

Deviation of residual pressure for several morphologies of an inclusion plotted versus the normalized aspect ratio. The deviation of residual pressure is quantified as ($P_{nonspherical}/P_{spherical} - 1$). The normalized aspect ratio is calculated with the unique axis as the denominator (e.g., the prolate ellipsoid 2:1:1 becomes ½ = 0.5). For a soft inclusion in a stiffer host (e.g., quartz-in-garnet), the deviation is negative, and therefore $P_{nonspherical} < P_{spherical}$. The opposite occurs for a stiff inclusion in a softer host (e.g., diamond-in-pyrope; $P_{nonspherical} > P_{spherical}$). Figure adapted with permission from Mazzucchelli et al. (2018) and Zhong et al. (2021a) (CC BY 4.0).

Aspect ratio most strongly controls the deviation of residual pressure, with the largest deviations expected for platy inclusions (**Figure 8**). Edges and corners further enhance deviations. In general, morphology is less important when the inclusion is softer than the host. For QuiG, or pyrope-in-diamond with aspect ratios less than 1:2:2, deviations induced by shape are typically less than 5% (**Figure 8**). For a stiff inclusion with the same shape in a soft host, the deviation is much larger (e.g., ∼20% for diamond-in-pyrope) and of the opposite sign. Approximating irregular inclusion shapes with 3D ellipsoids and calculating the stress of the resulting ellipsoid using the analytical Eshelby solution (Eshelby 1957) is accurate to ∼2% (Zhong et al. 2021a) and makes numerical modeling unnecessary for most applications. However, the geometry of the inclusion and its crystallographic orientation are still required.

These results provide a simple corrective procedure for nonspherical inclusions (Mazzucchelli et al. 2018). For example, if geometry introduces a 5% decrease in P_{inc}, [e.g., a pyrope crystal with aspect ratio of 2.0 included in diamond (**Figure 8**)], measured P_{inc} is increased by a factor of 1.0/0.95 and calculations proceed as for a spherical inclusion (Equations 3 and 4). More accurate

calculations require 3D models of the host-inclusion system (e.g., Anzolini et al. 2019, Alvaro et al. 2020, Zhong et al. 2021a). This approach accommodates all fundamental characteristics of the system, including any elastic anisotropy of the host and the inclusion, the relative orientation of the crystallographic axes of the host and the inclusion, the position of the inclusion with respect to other inclusions and to the external walls of the host, and the exact morphology of the inclusion and its orientation with respect to the crystallographic axes. Such models return the stress and strain fields in both the host and the inclusion, and their gradients, and are best suited for detailed studies where the strain state and the relative crystallographic orientation of the inclusion are known (e.g., Alvaro et al. 2020).

Proximity to Free Surfaces and Other Inclusions

The size of the inclusion and its proximity to the external surfaces can strongly affect the stress and strain distribution within and around an inclusion and thus the calculation of entrapment conditions (Rosenfeld & Chase 1961, Zhang 1998, Enami et al. 2007, Mazzucchelli et al. 2018, Zhong et al. 2020b). For small inclusions with $R_{host}/R_{inc} > 4$, P_{inc} is within 1% of the value expected for an infinite host, especially when the inclusion is relatively soft (e.g., QuiG), but deviations rapidly exceed 10% for $R_{host}/R_{inc} < 2$ (Mazzucchelli et al. 2018). The proximity of the inclusion to the external surface of the host is particularly crucial for high-pressure metamorphic rocks (high P_{inc}) that are investigated on less than 100-μm-thick sections. P_{inc} for a deeply embedded inclusion decreases as the distance from the specimen surface decreases (e.g., during grinding or polishing a thin section), although the pressure release is less for soft inclusions such as QuiG or garnet-in-diamond (**Figure 9**). To minimize pressure release in the entire inclusion (<3%), the inclusion depth (D_{inc}) normalized over its radius (R_{inc}) should exceed 2–2.5; stiffer inclusions (e.g., garnet-in-quartz or ZiG) should be buried deeper ($D_{inc}/R_{inc} \geq \sim 4$) (Mazzucchelli et al. 2018, Zhong et al. 2020b) (**Figure 9**). Nearly exposed inclusions develop large pressure and strain gradients,

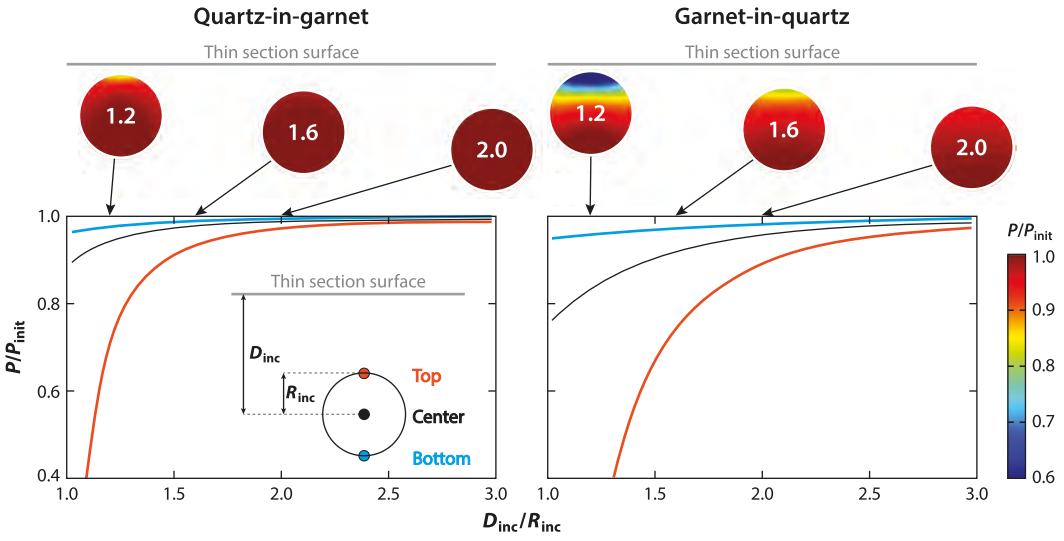

Figure 9

Numerical models of pressure distribution across an inclusion versus distance (D_{inc}) from a thin section surface, normalized to initial (homogeneous) inclusion pressure (P_{init}) and inclusion radius (R_{inc}). The top versus bottom of the inclusion are highly sensitive versus insensitive to proximity. Proximity matters less for stiffer hosts (garnet) than for softer hosts (quartz). Figure adapted with permission from Zhong et al. (2020b) (CC BY 4.0).

so analytical placement matters. For example, P_{inc} at the bottom of a nearly exposed inclusion ($D_{inc}/R_{inc} = 1.2$) is still within 5% of a deeply buried inclusion (Mazzucchelli et al. 2018, Zhong et al. 2020b).

Experiments support these models but also reveal discrepancies. Campomenosi et al. (2018) collected Raman spectra on zircon inclusions initially entrapped in garnet at the center of a thick section during several steps of polishing to expose the inclusion. As expected, the Raman shift (and therefore the strain and stress) of the inclusion decreased as the external surface of the section approached the inclusion. However, even when the inclusion was exposed at the surface, it still exhibited a peak shift compared to a free crystal, implying the residual strain and stress were not completely released. This result accords with electron backscatter diffraction measurements on olivine and quartz that also indicate residual stresses, even for fully exposed crystals (Wallis et al. 2019). In consequence, Campomenosi et al. (2018) recommend against using exposed crystals in a thin section as supposed strain and stress free standards. Instead, free, unstrained, polished crystals (e.g., Herkimer quartz, Mud Tank zircon, synthetic crystals, etc.) are preferred. Comprehensive numerical simulations of the experiment (Campomenosi et al. 2018) further showed that anisotropic elastic properties, geometry, and crystallographic orientation of the inclusion all strongly influence stress release. However, nonelastic processes also contributed to stress release as the polished surface intersected the inclusion. In particular, the high differential stress in the host around the inclusion (**Figure 9**) localized plastic yield and further released the pressure of the inclusion.

Little work has yet been published on the effect of mutual proximity of inclusions, but stress interactions can occur if inclusions are closely crowded and/or of unequal size (Zhong et al. 2021a; M.L. Mazzucchelli, unpublished modeling). Inclusions with similar radii show little stress interaction unless they are separated by a small fraction of the inclusion radius (Zhong et al. 2021a). More generally, modeling the effects of free surfaces (Mazzucchelli et al. 2018, Campomenosi et al. 2018, Zhong et al. 2020b) suggests distances between the centers of two inclusions should be at least 2–4 times the radius of the larger inclusion; otherwise, stress interactions are likely. Exact analytical placement matters, however, and portions of an inclusion farthest removed from surfaces or other inclusions are more likely to retain undisturbed P_{inc} (Mazzucchelli et al. 2018; Zhong et al. 2020b, 2021a) (**Figure 9**).

MODEL REFINEMENT 2: ACCOUNTING FOR ELASTIC ANISOTROPY

The strain and stress fields in a crystal reflect both the stress distribution from the surrounding environment and the crystal's elastic properties. For example, if a crystal is immersed in a liquid, it will experience hydrostatic stress and the crystal (inclusion) will develop isotropic or anisotropic strains depending on its symmetry and its elastic properties. The response of a crystal to hydrostatic stress is governed simply by its second-rank compressibility tensor (Nye 1985). However, if the crystal (inclusion) is entrapped within another solid material (host), it will be subjected to strains arising not only from the external stress conditions but also from the elastic properties of the host material. In this case, the stress response of the inclusion is governed by its fourth-rank stiffness tensor. **Figure 10** shows a simplified geometrical interpretation of the behavior of an elastic host-inclusion system with different combinations of elastic anisotropy of its minerals. To simplify discussion, we assume the inclusion is spherical when entrapped, the host is infinite, and the external stress is homogeneous and hydrostatic both at entrapment and at room pressure. Now we remove the inclusion from the host and bring both the host and inclusion to room conditions. Both crystals will expand according to the behavior of free crystals under hydrostatic pressure. If both crystals are elastically isotropic or cubic, both the cavity in the host and the inclusion remain

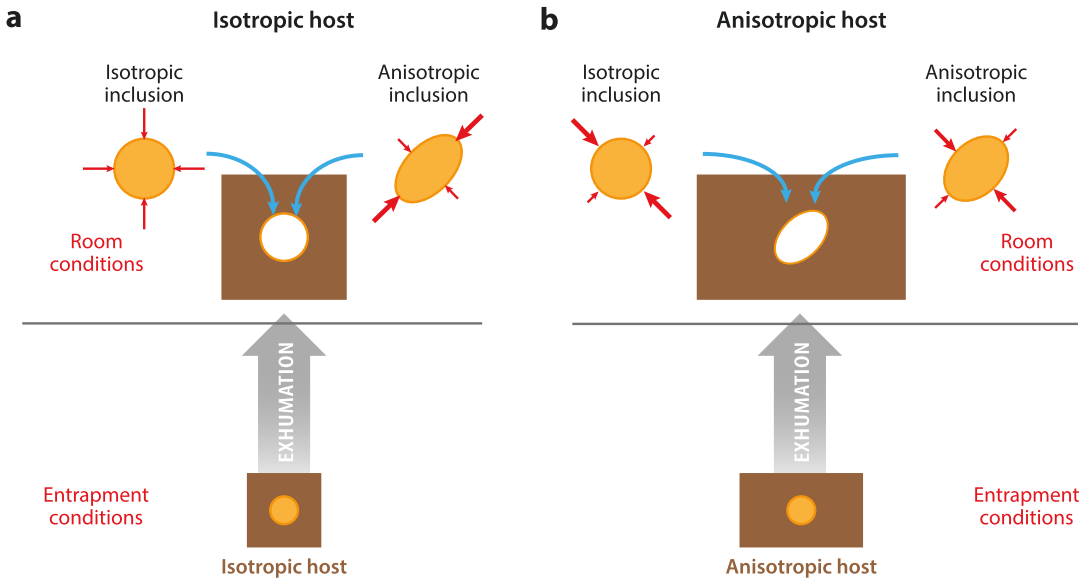

Figure 10

Schematic illustration of stresses on an originally spherical inclusion after exhumation of the host from entrapment to room conditions. (*a*) If the host is isotropic or cubic, the spherical cavity remains spherical after exhumation. The stress required to force an inclusion into the cavity is isotropic for an elastically isotropic inclusion (*upper left*) but anisotropic for an elastically anisotropic inclusion (*upper right*). (*b*) If the host is elastically anisotropic, the shape of the cavity changes upon exhumation. In this case, the stress required to push the inclusion back into the cavity is anisotropic, even when the inclusion is elastically isotropic. Figure adapted with permission from Mazzucchelli et al. (2019).

spherical, and an isotropic stress (i.e., a hydrostatic pressure) is required to force the crystal back into the cavity (**Figure 10*a***). The inclusion must therefore experience hydrostatic stress. If the inclusion is anisotropic, however, it will expand more in one direction than another and become ellipsoidal at room pressure (**Figure 10*a***). An anisotropic stress is then required to fit the inclusion into the spherical cavity of the cubic host. Although elastic interaction between host and inclusion will deform the cavity so that it is no longer spherical, stresses will nonetheless be anisotropic around and within the trapped inclusion. For an anisotropic host, an isotropic inclusion will remain spherical when recovered to room conditions but will require anisotropic stress to force it into the ellipsoidal cavity developed on exhumation (**Figure 10*b***). When both phases are anisotropic, the stress required (**Figure 10*b***) depends on the mutual crystallographic orientation of the host and inclusion. In this case the strains developed may decrease (break) the symmetry of the inclusion.

The residual strain and stress of anisotropic inclusions can be calculated if P_{trap}, T_{trap}, the elastic properties of host and inclusion, and the geometry of the system are known (Mazzucchelli et al. 2019; Zhong et al. 2019b, 2021a; Morganti et al. 2020; Gonzalez et al. 2021). First, the lattice strains of the host and inclusion at P_{trap}, T_{trap} are calculated. Second, the host is brought to reference conditions, the shape of the cavity is calculated, and the inclusion is stressed to fit into the cavity. At this point, mechanical equilibrium has not been achieved because the inclusion is stressed to match the geometry of the cavity, while the host itself is stress free. This condition is comparable to **Figure 6*c***, except that the magnitude of the stress step may vary with location along the inclusion-host boundary [anisotropic cases (**Figure 10**)]. Finally, elastic interaction is calculated (comparable to **Figure 6*d***), changing the stress and strain states of both the host and

the inclusion. In this step, the shape of the inclusion must be accounted for. The strain and stress obtained after this calculation represent the final residual strain and stress of the inclusion.

Two different approaches have been proposed for the first steps in the calculation (prior to elastic interaction). Zhong et al. (2019b, 2021a) used the elastic stiffness tensor to determine the stress and strain state of the host and inclusion. This approach permits either a hydrostatic or nonhydrostatic external stress field, but it also requires knowledge of the stiffness tensors for the host and inclusion, as well as their stress (or at least pressure) and temperature dependencies. This information is rarely available, especially for the P-T ranges required for elastic barometry calculations. Calculations so far have assumed constant elastic properties determined at room conditions (Zhong et al. 2019b, 2021a). Mazzucchelli et al. (2019) calculated strains prior to elastic interaction using the volume and axial EoSs of the two minerals. For minerals belonging to the cubic crystal system, a single-volume EoS is sufficient for modeling hydrostatic conditions because the compressibility and thermal expansion tensors are isotropic. Uniaxial crystals (tetragonal, trigonal, hexagonal systems) have two independent lattice parameters, so two EoSs are required to describe their strains. More EoSs are required for crystals with lower symmetry (Angel et al. 2021). The advantage of models based on the volume and axial EoS is that the lattice strain can be calculated at geologically relevant P and T using a fully parameterized and experimentally validated model (the EoS). However, calculations are limited to a hydrostatic external stress field. Gonzalez et al. (2021) showed how axial and volume EoS in anisotropic elastic calculations can be applied to lower crystallographic symmetries by using the concept of a deformation gradient tensor, but calculations still require hydrostatic external stress.

The elastic interaction (final calculation) is essentially an eigenstrain problem. If the host is elastically isotropic and the inclusion is ellipsoidal, Eshelby's equivalent inclusion method (Eshelby 1957) can be used to calculate the deformation of the inclusion analytically. The calculation is based on the Eshelby tensor, which depends on the shape of the inclusion, the elastic properties of the isotropic host, and the elastic properties of the inclusion, which may be elastically anisotropic (Eshelby 1957, Mura 1987). In fact, analytical solutions that describe the effect of the morphology of the inclusion (Zhong et al. 2021a) (**Figure 8**) are all based on Eshelby's equivalent inclusion method. However, the host mineral cannot be perfectly elastically isotropic (even cubic minerals exhibit different stiffnesses in different crystallographic directions, e.g., along <1 1 1> versus <1 0 0>), and the inclusion may not be an isolated ellipsoid. Consequently, complete predictive accuracy requires a full numerical mechanical calculation (e.g., Mazzucchelli et al. 2019, Morganti et al. 2020, Zhong et al. 2021a), which can then include the elastic anisotropies of the two minerals, their relative crystallographic orientations, and the inclusion shape. While very flexible, this approach requires a new calculation whenever any one parameter is changed, i.e., every specific initial entrapment condition would require a new calculation. To relieve the need for numerical simulations, Mazzucchelli et al. (2019) and Morganti et al. (2020) introduced the so-called relaxation tensor, which transforms the unrelaxed strain into relaxed strain (and vice versa). The components of the relaxation tensor are calculated numerically for the specific elastic properties, geometry, and relative orientation of a host-inclusion pair (e.g., QuiG, assuming spherical geometry). Once calculated, the relaxation tensor can be applied to calculate the elastic interaction for that system for any entrapment conditions, with no need for further numerical modeling.

Isotropic Host, Anisotropic Inclusion

Strictly speaking, all minerals are elastically anisotropic (Nye 1985), but practically speaking, cubic minerals can usually be approximated as quasi-isotropic (Mazzucchelli et al. 2019). Strict calculations show that the residual strain and stress in the inclusion are isotropic when the following three

conditions are met: (*a*) both the host and inclusion are crystallographically cubic, (*b*) the inclusion is spherical, and (*c*) the external stress is hydrostatic (Mazzucchelli et al. 2018, 2019). Increasing axial anisotropy results in increasingly anisotropic residual strains and stresses, with differential stresses (along different crystallographic axes) reaching a few kilobars (Mazzucchelli et al. 2018, 2019; Zhong et al. 2018, 2021a). For garnet hosts, and assuming a simple geometry of the system, the anisotropic model and the isotropic model predict similar residual volume strains and P_{inc}. The differences between the predictions of isotropic versus anisotropic models are usually comparable to the typical propagated measurement uncertainties arising from X-ray diffraction or Raman spectroscopy. Moreover, when the host is quasi-isotropic, the strain of a spherical inclusion does not change with the relative crystallographic orientation as demonstrated for inclusions with a wide range of stiffness and anisotropy in garnet (Mazzucchelli et al. 2018, 2019; Zhong et al. 2021a). Therefore, for isolated quasi-spherical inclusions in garnet, diamond, or other cubic crystals, relative orientation is not necessary to constrain entrapment conditions. However, relative crystallographic orientation should be determined when modeling irregular, highly stretched, or highly flattened inclusions (Zhong et al. 2021a,c).

Alvaro et al. (2020) showed that the anisotropic model can, in principle, be inverted to estimate unique conditions of either entrapment or mechanical closure. The individual axis-specific strains are measured for an inclusion using X-ray diffraction or Raman spectroscopy, and the effect of the elastic interaction is computed with a numerical model that includes the specific geometry of the inclusion and the elastic anisotropy and crystallographic orientation of the minerals in the system. The strain state of the inclusion corrected for the elastic interaction is then used together with the volume and axial EoS to calculate axial (axis-specific) isomekes, one for each independent crystallographic direction in the crystal. Each axial isomeke represents the P and T conditions at which the strains of the host and inclusion, as calculated along a specific crystallographic direction, are equal. For QuiG without symmetry breaking there are two independent directions, corresponding to the *a*- and *c*-crystallographic axes in quartz, and therefore two P-T lines are calculated. The intersection of these two lines provides a unique possible P and T of entrapment or mechanical closure for each inclusion. The method does assume that external stress is hydrostatic.

As applied to an eclogite xenolith from the Mir kimberlite (Yakutia, Russia), the method returns P-T conditions of ∼900°C, ∼30 kbar (Alvaro et al. 2020) (**Figure 11**). This P-T condition falls toward the low P-T end of xenoliths from the Mir kimberlite (Ashchepkov et al. 2010) but is much higher than expected for prograde growth of garnet along the subduction path of a crustal protolith and is generally hotter than typical subduction geotherms (Penniston-Dorland et al. 2015) (**Figure 11**). At 900°C, garnet viscously relaxes on timescales of ∼1 to 1,000 years (Zhong et al. 2020b), so this P-T condition likely represents postentrapment reequilibration of quartz inclusions via viscous flow near the peak of metamorphism. Within uncertainty, the rock could have remained in the quartz stability field (Osborne et al. 2019). Subsequent eruption of the kimberlite was sufficiently rapid [kimberlites can ascend 200 km in ∼1 h (Russell et al. 2019)] to prevent further significant resetting of the inclusion stress state.

Anisotropic Host and Inclusion

Mineral inclusions are often contained within significantly anisotropic host minerals, in which case nonhydrostatic residual stresses may develop in the inclusion (**Figure 10*b***). Often, simple isotropic models have been applied to nonisotropic host minerals, such as quartz-in-epidote (Cisneros et al. 2020), apatite-in-zircon (Guo et al. 2021), and coesite-in-kyanite (Taguchi et al. 2019). These models implicitly assume that elastic anisotropy and relative orientation are negligible. Gonzalez et al. (2021) tested this assumption for QuiZ by using volumetric and axial EoS for both host and

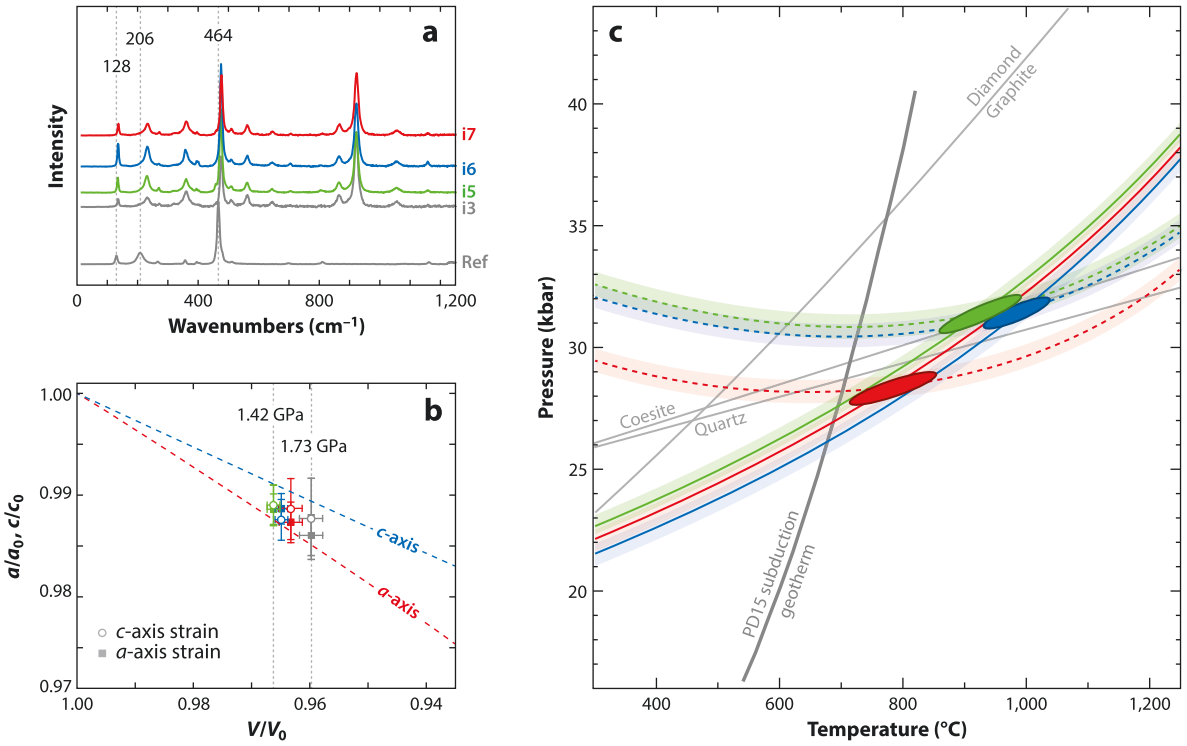

Figure 11

(*a*) Raman spectra measured on four quartz inclusions entrapped in garnet host from an eclogite xenolith, Mir kimberlite pipe (Yakutia, Russia). (*b*) Residual strains (a/a_0 and c/c_0) along *a*- and *c*-axes (*squares* and *circles*, respectively) are isotropic within estimated standard deviations after correcting for anisotropic elastic relaxation. Dashed lines represent hydrostatic equations of state for *a*- and *c*-axes of quartz. Two boundary values of inclusion pressure correspond with V/V_0 value. (*c*) P-T plot with axial isomekes for the *a*-axis (*solid lines*) and *c*-axis (*dashed lines*). Shading represents uncertainties on measurements. Intersection between axial isomekes represents the unique P-T condition of elastic equilibration, assuming hydrostatic conditions. Ellipsoids represent 2σ uncertainties in intersection position. Calculations for inclusion i3 (*gray*) are indistinguishable from inclusion i5 (*green*). Figure adapted with permission from Alvaro et al. (2020). The coesite-quartz boundaries are from Bose & Ganguly (1995) and Osborne et al. (2019).

the inclusion to evaluate how their lattice parameters change during exhumation. Elastic interaction was evaluated numerically for diverse orientations using the concept of a relaxation tensor. Their results showed that the strain developed in the inclusion upon exhumation is anisotropic, and the value of the individual components is a function of both the entrapment conditions and relative crystallographic orientations. If the *c*-axes of both minerals are aligned, the residual strain developed in the quartz inclusion preserves its trigonal symmetry. However, all other orientations induce shear strains that reduce the symmetry of the quartz inclusion to triclinic. Orientation also affects the volume strain and the residual pressure in the inclusion. Nonetheless, the maximum discrepancy between isotropic and fully anisotropic models is less than 600 bars for both P_{trap} (22 kbar; **Figure 12**, shown explicitly) and P_{inc} (~8 kbar; not illustrated), suggesting that the isotropic elastic model for QuiZ is accurate to within a few percent. However, axial deviations can reach nearly 2 kbar, depending on which Raman modes are used (Murri et al. 2022), and may be larger for more elastically discrepant host-inclusion pairs. Models for minerals with lower symmetry (orthorhombic, monoclinic, triclinic) have not been developed and could potentially compare less favorably with isotropic models.

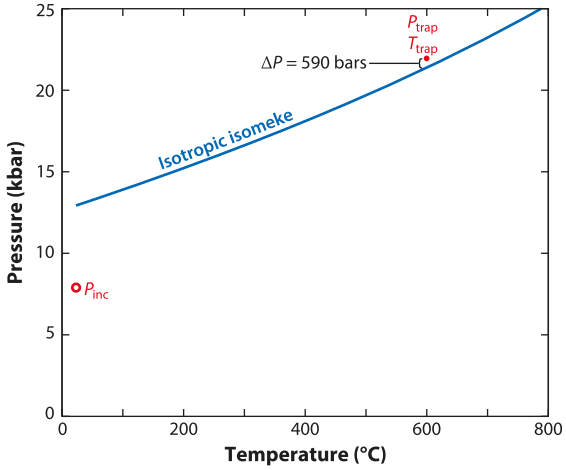

Figure 12

Entrapment isomeke for quartz-in-zircon calculated using the isotropic model together with the residual strain of a quartz inclusion in a zircon host. The residual strain was calculated with an anisotropic calculation taking as entrapment conditions 22 kbar and 600°C (*red dot*). The maximum discrepancy on the entrapment pressure is less than 600 bars. Figure adapted with permission from Gonzalez et al. (2021).

How Anisotropy Breaks Crystallographic Symmetry

As discussed previously, the Grüneisen tensor is used to calculate axial strains from Raman peak shifts. As a second-rank symmetric property tensor, the Grüneisen tensor is subject to the symmetry of the crystal (Ziman 1960, Angel et al. 2019). Symmetry is preserved when the inclusion is spherical, the host is elastically isotropic, and the external stress acting on the host is hydrostatic. However, when the host-inclusion system is fully anisotropic (e.g., QuiZ), the symmetry of the inclusion can be broken upon exhumation, modifying the phonon modes (Raman peak positions). Murri et al. (2022) used DFT and elastic calculations to investigate the QuiZ system, for which symmetry-breaking residual strains are expected in the inclusion. Specifically, they tested whether significant errors in strains and mean stresses arise when using the unbroken (incorrect) phonon-mode Grüneisen tensor of trigonal α-quartz to calculate the inclusion strains (**Figure 13**). Their results show that the changes in Raman peak positions for real quartz inclusions in zircon are similar to expectations if the quartz inclusions remained truly trigonal in symmetry. Very large symmetry-breaking strains induce peak broadening or even splitting (for E modes). For small strains, the simple trigonal Grüneisen tensor can be used to calculate the average inclusion pressures with errors ranging from 3% to 10%. However, the trigonal Grüneisen tensor introduces significant errors for axial strains and placement of axial isomekes (**Figure 13**). Application of the approach of Alvaro et al. (2020) often results in axial isomekes that do not intersect and cannot recover a unique P_{trap}, T_{trap} (**Figure 13*b***).

Does Anisotropy Matter?

Elastically anisotropic minerals dominate Earth, so inclusion strains should commonly be anisotropic and stresses nonhydrostatic. For QuiG, application of simple hydrostatic calibrations to calculate P_{inc} from Raman shifts to a single peak (e.g., equations from Schmidt & Ziemann 2000, Enami et al. 2007, Ashley et al. 2014, Kohn 2014, Thomas & Spear 2018, etc.) can lead to errors in back-calculated entrapment pressures that exceed 10 kbar for experiments up to 30 kbar (Bonazzi et al. 2019), although many errors are smaller (c. 1 kbar). Accounting for strain and

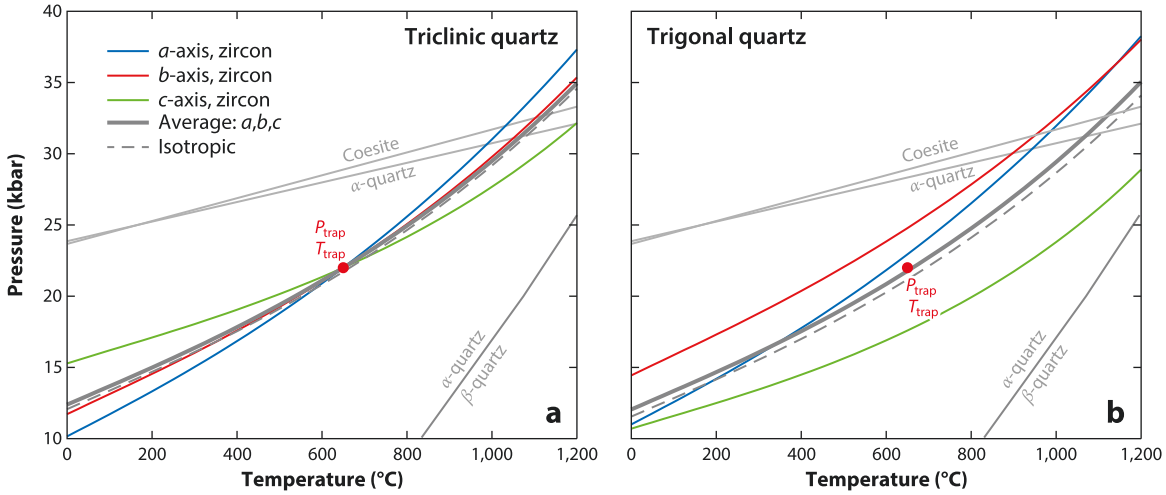

Figure 13

Axial and volume isomekes calculated based on the residual strain of a quartz inclusion in zircon for a model eclogite. Axial isomekes are calculated using the anisotropic model of Alvaro et al. (2020) and Gonzalez et al. (2021) for the directions of the *a*-, *b*-, and *c*-axes of the zircon host and their corresponding directions in the quartz inclusion. The isotropic isomeke is calculated from the volume strain of the inclusion using the isotropic model. (*a*) Entrapment isomekes using the true symmetry-broken (triclinic) strains intersect at P_{trap}, T_{trap}. (*b*) Entrapment isomekes using strains calculated from the (incorrect) trigonal Grüneisen phonon-mode tensor do not intersect at P_{trap}, T_{trap}. Figure adapted with permission from Murri et al. (2022).

stress anisotropy to determine P_{inc} reproduces experiments, even when stresses are nonhydrostatic (Bonazzi et al. 2019), and is most accurate. Ab initio DFT calculations (Murri et al. 2022) further show that, at least for quartz inclusions, the measured Raman shifts can be used to calculate P_{inc}, even when the inclusion is subjected to symmetry-breaking strains. Once P_{inc} is determined, however, the differences between isotropic versus anisotropic calculations are typically comparable to uncertainties on the measurements of strain in natural inclusions with X-ray diffraction or Raman spectroscopy. Discrepancies are also small (typically less than 1 kbar) for the fully anisotropic QuiZ system.

Anisotropy is especially crucial to the method of Alvaro et al. (2020) to determine P_{trap}, T_{trap} from a single inclusion. These calculations require consideration of elastic anisotropy (also inclusion shape and orientation), and rely on the axial and volume EoS of the minerals to describe how unit-cell parameters change with temperature and hydrostatic pressure. Calculations must therefore assume entrapment or mechanical closure occurred at hydrostatic conditions. The lack of the full anisotropic elastic properties and their variation with stress and temperature at conditions relevant for metamorphic rocks currently prevent calculations for nonhydrostatic stresses.

INELASTIC PROCESSES

As a residual pressure develops in an inclusion, gradients in radial and tangential stresses develop in the host (Equations 1 and 2; **Figure 5**) and can drive plastic yield, fracturing, and viscous creep. All these processes can modify the value of P_{inc} compared to purely elastic models. Although elastic strain disappears after stress is removed, plastic yield, fracturing, and viscous relaxation are irreversible. Therefore, the strain developed in a visco-elasto-plastic system is path dependent—it depends not only on the initial (entrapment) and the final P-T conditions but also on the entire stress-strain-temperature history (e.g., Zhong et al. 2018).

Following the mechanical literature, we distinguish time-independent plastic yield and fracturing from time-dependent viscous creep (Zhang 1998; Zhong et al. 2018, 2020b). Plastic deformation of the host occurs whenever the differential stress exceeds a threshold, called the yield strength (e.g., Zhang 1998). Using the Tresca criterion, plastic yield occurs when

$$\left|\sigma_{\text{tangential}} - \sigma_{\text{radial}}\right| \geq Y_{\text{host}}, \quad 5.$$

where $|\sigma_{\text{tangential}} - \sigma_{\text{radial}}|$ is the differential stress in the host around the inclusion (see **Figure 5**), and Y_{host} is the yield strength of the host mineral. The yield criterion might be reached if a pressure differential already exists between host and inclusion and temperature increases (decreasing Y_{host}) and/or if pressure differential increases along a P-T path. Plastic strain in the host then occurs, which limits the magnitude of the differential stress in the host and, ultimately, the inclusion pressure. Plastic deformation stops as soon as the differential stress falls under the threshold limit. This process does not completely relax the stress, but P_{inc} no longer conforms to an elastic model of entrapment.

Mode I fractures propagate when the stress intensity factor at the tip of a crack, that is related to the pressure difference $|P_{\text{inc}} - P_{\text{host}}|$, exceeds the host fracture toughness (Zhang 1998, Whitney et al. 2000). Crack propagation increases the volume of the cavity and decreases the pressure in the inclusion (e.g., van der Molen & van Roermund 1986, Puhan 2021). Positive (compressive) residual stresses drive radial fracturing, e.g., around coesite inclusions in garnet partially retrogressed to quartz (Chopin 1984) (**Figure 1*f***), quartz inclusions in pyroxene (van der Molen & van Roermund 1986), and olivine and sulfide inclusions in diamond (e.g., Harris 1972). Tensile stresses drive tangential fracturing [e.g., olivine in feldspar (van der Molen & van Roermund 1986)].

Viscous creep responds to differential stress in the host mineral and is a function of time. In an infinite amount of time, all residual pressure would vanish and become equal to the far-field pressure acting on the host. Effective viscosity represents a key parameter to describe this viscous relaxation (Dabrowski et al. 2015, Zhong et al. 2020b):

$$\eta_{\text{host}} = A|\tau_{\text{rr}}|^{1-n}, \quad 6.$$

where τ_{rr} is the radial component of the deviatoric stress, A is an exponentially temperature-dependent prefactor, and n is the stress exponent. In the simplest case of a spherical inclusion and linear (Newtonian) viscoelasticity (i.e., $n = 1$ in Equation 6), the time-dependent relaxation of P_{inc} is (Dabrowski et al. 2015)

$$P_{\text{inc}}(t) = P_{\text{host}} + (P_{\text{inc},0} - P_{\text{host}})\, e^{\left(-\frac{3K_{\text{inc}}}{4\eta_{\text{host}}}t\right)}, \quad 7.$$

where $P_{\text{inc},0}$ is the initial pressure of the inclusion at time $t = 0$, P_{host} is the far-field pressure on the host, η_{host} is the viscosity of the host, and K_{inc} is the bulk modulus of the inclusion. The characteristic relaxation time is $\frac{4\eta_{\text{host}}}{3K_{\text{inc}}}$ (Zhang 1998, Dabrowski et al. 2015). Importantly, relaxation is scale independent, so all inclusions with the same $P_{\text{inc},0}$ in a host will relax at the same rate, regardless of inclusion size. When $n > 1$ in Equation 7 (non-Newtonian material), pressure relaxation generally slows, but response remains scale independent (Dabrowski et al. 2015, Zhong et al. 2020b). The rate of relaxation depends strongly on $|P_{\text{inc}} - P_{\text{host}}|$, however, and for QuiG, a 10-kbar differential stress relaxes 1,000 times faster than a 1-kbar differential stress (Zhong et al. 2020b).

In a 1D visco-elasto-plastic mechanical model of a spherical inclusion in an infinite host (Zhong et al. 2020b), nondimensionalization reveals two particularly useful parameters. The Deborah number (*De*) is a dimensionless time that ratios the characteristic viscous relaxation time of the host with the model duration (analogous to the characteristic time at elevated temperature for a natural system). Dimensionless yield strength (C^*) ratios yield strength of the host with P_{inc} to determine the resistance of the host to plastic yielding. For QuiG at constant temperature and

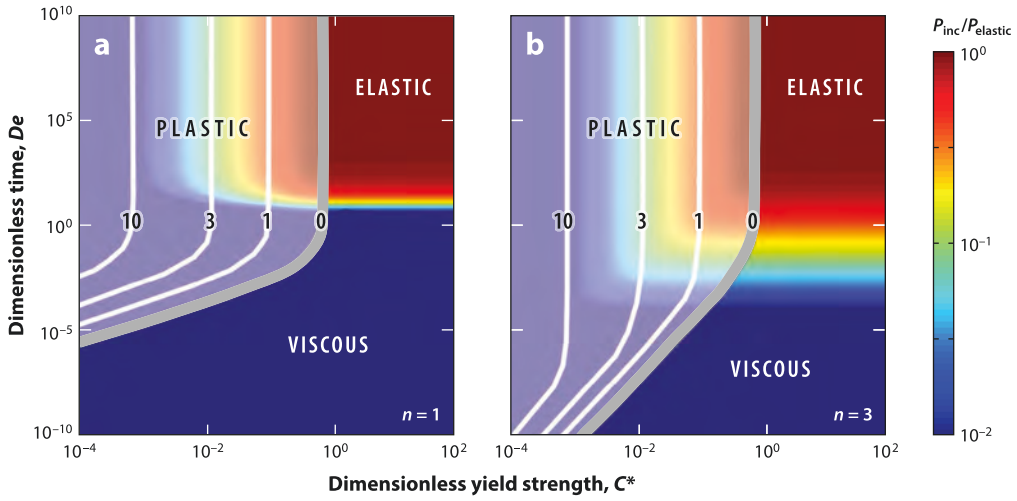

Figure 14

Simple models of relaxation assuming constant initial P_{inc}, P_{host}, and temperature, depicted on a plot of dimensionless time (Deborah number, *De*) versus dimensionless yield strength (C^*). Results are colored according to predicted final P_{inc} divided by the pressure expected for purely elastic behavior ($P_{elastic}$), and contoured for the ratio of the radius of the plastic yield region to inclusion radius (*white* and *gray lines*). The thick gray line represents the onset of plastic yield. Three regimes are evident: (1) elastic ($De > \sim 2$, $C^* > 1$); (2) viscous ($De < \sim 1$ and C^* to the right of the *gray line*); and (3) plastic (to the left of the *gray line*; *lighter shading*). (*a*) $n = 1$ in Equation 6 (effective viscosity expression). (*b*) $n = 3$ in Equation 6. Figure adapted with permission from Zhong et al. (2020b) (CC BY 4.0).

$P_{host} = 1$ bar, three regimes can be mapped onto *De* versus C^* space (**Figure 14**). An elastic rheology prevails (elastic in **Figure 14**) when $De > \sim 2$ and $C^* > 1$. P_{inc} does not relax by viscous creep or plastic yield and retains a value predicted for purely elastic behavior ($P_{elastic}$). A viscous regime dominates when $De < 1$, and C^* exceeds the onset of plastic yield. In this region, P_{inc} decreases because of viscous creep. Larger stress exponents ($n \sim 3$ for most rock and mineral deformation experiments) reduce the extent of the viscous regime. A plastic regime prevails at low C^* and high *De* (to the left of the gray curves in **Figure 14**), and P_{inc} decreases because of plastic yield.

The viscosity of minerals decreases at high temperature. At low temperatures, the characteristic viscous relaxation time (and, as a consequence, *De*) increases, preventing viscous relaxation. Therefore, plastic yielding is more likely than creep at low temperatures. However, many common host minerals such as garnet and diamond have high yield strength at ambient conditions, which limits the amount of plastic relaxation. For example, observations of Whitney et al. (2007) imply a yield strength of garnet between 4.4 and 5 GPa at ambient conditions. A high residual inclusion pressure of 10 kbar leads to $C^* \sim 4.4$–5, outside the plastic yield region (**Figure 14**). Therefore, plastic yield should not be expected for garnet and diamond hosts, unless high differential stress develops locally, e.g., around the corners of faceted inclusions or during polymorphic transitions with large volume changes, such as quartz-coesite (**Figure 1*f***).

Longer durations at higher temperatures decrease *De* and promote viscous relaxation. For example, P_{inc} for a quartz inclusion entrapped in garnet at 700°C within the eclogite facies might be lower by ~10% if exhumation requires 1 Myr and 20% for 10 Myr (Zhong et al. 2020b; see also Dabrowski et al. 2015). Increasing temperature to 800°C would reduce final P_{inc} by 30–35% (Zhong et al. 2020b). If an elastic model is used to interpret the reduced P_{inc}, apparent P_{trap} or T_{trap} will be miscalculated (underestimated for inclusions with positive P_{inc}). Some studies indeed show that P_{inc} for inclusions entrapped in metamorphic garnets at $T > 650$°C are less than elastic models predict (e.g., Korsakov et al. 2009; Campomenosi et al. 2021). However, rapid cooling

(high *De*) promotes preservation of P_{inc}, even for high-temperature entrapment, as confirmed theoretically (e.g., Zhong et al. 2018), empirically for xenoliths (Alvaro et al. 2020), and experimentally (Thomas & Spear 2018; Bonazzi et al. 2019).

Inelastic relaxation along a metamorphic P-T path can be complicated. As P-T conditions change, P_{inc} attempts to approach the external pressure, but depending on the exact history, P_{inc} may be only partially or completely relaxed (Zhong et al. 2020b, Campomenosi et al. 2022). Plastic or viscous relaxation can occur on both the prograde and retrograde paths, either partially or completely to a mechanical closure temperature. Therefore, an elastic interpretation of P_{inc} might overestimate or underestimate either the true entrapment conditions or the metamorphic peak conditions (or both). Unlike diffusion-controlled closure, which depends almost exclusively on temperature, reequilibration and mechanical closure of inclusions depend additionally on rates of change in P_{inc}, its magnitude, and sign (Zhong et al. 2020b, Campomenosi et al. 2022). For example, two rocks that reached ~745 and 880°C at 12 kbar record near-peak ZiG temperatures (Kohn 2016, Gilio et al. 2021), whereas ZiG temperatures were reset from ~725 to 600–650°C for a ultra-high-pressure (UHP) rock that equilibrated at 30–40 kbar (Campomenosi et al. 2021). These differences likely reflect exhumation P-T paths, which produced tensile stresses around UHP inclusions but compressional stresses for the lower-pressure rocks (Campomenosi et al. 2022). Discrepancies inferred from elastic barometry versus phase equilibria arising from inelastic relaxation of inclusion pressures might be misinterpreted as thermal overstepping of crystal nucleation (Moulas et al. 2020, Zhong et al. 2020b) if chemistry is less affected at elevated temperature (e.g., if garnets are large).

EXAMPLES AND IMPLICATIONS

Thermobarometry

How accurate are past conventional thermobarometric estimates of P-T conditions and the methods we use to determine them? Although much work has considered the internal consistency of different thermodynamically based methods, a truly independent assessment has been lacking. Thus, one of the simplest but most important applications of elastic thermobarometry is in comparison with conventional, thermodynamically based thermobarometry.

In many cases, correspondence between calculated P-T conditions falls within error of both methods (**Figure 15**). Early work by Endo et al. (2012) represents the first comprehensive comparison and showed overlapping pressures at an assumed temperature using multiple thermodynamic methods and QuiG geobarometry (**Figure 15*a***). Kohn (2016) also showed good correspondence between pressures estimated using QuiG barometry (also ZiG thermometry) and thermodynamic methods (**Figure 15*b***). Although these older studies used simple models that have been superseded, recalculation nevertheless yields similar results, and more recent work by Wolfe & Spear (2020; also unpublished work from the authors) generally shows good correspondence (**Figure 15*b***). However, many estimates of garnet nucleation pressure from inclusions in cores of garnets are inconsistent with thermodynamic models (**Figure 15*b***), which has been interpreted to reflect chemical disequilibrium during garnet nucleation (Spear et al. 2014, Castro & Spear 2017). Rocks that exceeded 800°C show major reequilibration, both texturally (faceted inclusions) and in P_{inc} (**Figure 15*b***), and are interpreted to reflect thermally induced grain-boundary diffusion and viscous relaxation (Cesare et al. 2021). These discrepancies have promoted new research on nucleation energetics and reequilibration.

Reaction Overstepping

Discrepancies between thermodynamically versus elastically calculated pressures (using QuiG) for garnet cores led Spear and coworkers to propose that garnet nucleation is often overstepped

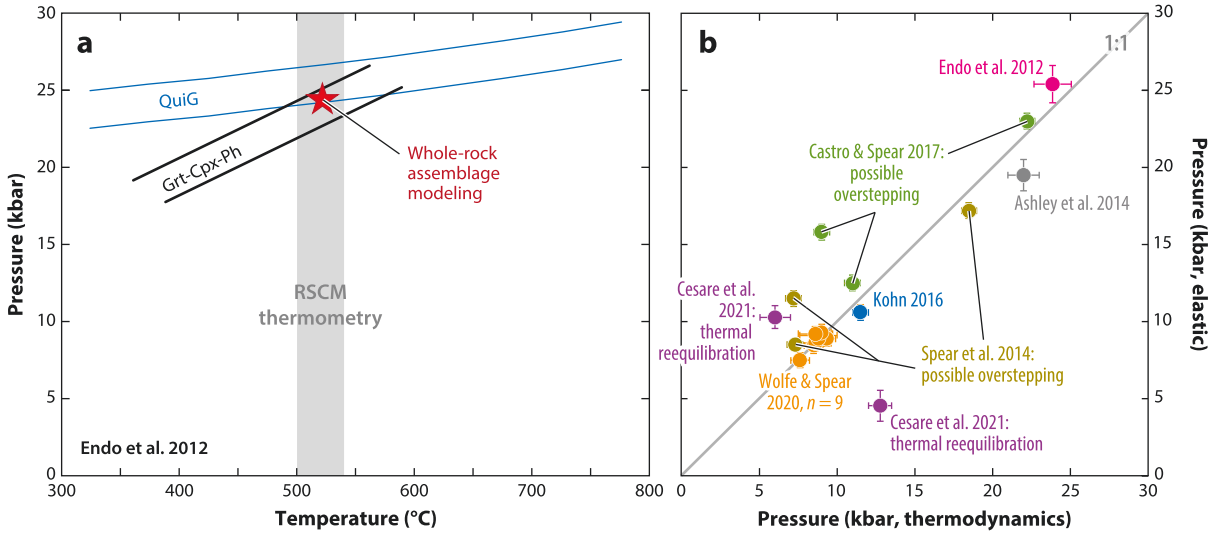

Figure 15

Comparison of pressures calculated using elastic thermobarometry versus thermodynamic methods (both thermobarometry and whole-rock chemical modeling). (*a*) Thermobarometric analysis of Endo et al. (2012) for eclogites from Guatemala, showing good correspondence between thermodynamic methods (Grt-Cpx-Ph equilibria; *red star* for thermodynamic modeling of whole-rock assemblages and mineral compositions) and elastic thermobarometry [quartz-in-garnet (QuiG)]. Preferred temperatures are from Raman spectroscopy of carbonaceous material (RSCM). (*b*) Many rocks yield similar results, but positive and negative barometric disparities in studies by Spear et al. (2014) and Castro & Spear (2017) have led to interpretations that garnet nucleation is substantially overstepped. In these cases, pressure determined using elastic thermobarometry is interpreted to be correct, and thermodynamically calculated pressure is interpreted to reflect chemical disequilibrium (see also **Figure 16**). QuiG also reequilibrates for high-temperature rocks (T > 800°C) (Cesare et al. 2021). Elastic pressure by Kohn (2016) has been recalculated using more recent methods.

(Spear et al. 2014, Castro & Spear 2017, Wolfe & Spear 2020). We do not discuss the energetic requirements for nucleation in detail here (see Gaidies et al. 2011, Pattison et al. 2011), but basically contribution of surface free energy displaces mineral nucleation to higher pressures or temperatures than the equilibrium isograd. Overstepping is required to overcome this surface free energy contribution, but the magnitude of overstepping, which directly translates into the volume of a mineral core that grows out of thermodynamic equilibrium with the matrix, remains unknown. Unfortunately, the sense of chemical zoning cannot generally distinguish whether a crystal has grown via overstepping or in equilibrium (Spear 2017).

Castro & Spear (2017) provide the strongest evidence for garnet nucleation overstepping. Their work on the Cyclades subduction complex shows major discrepancies among equilibrium thermodynamic models, petrography, and independent thermobarometry. For example (**Figure 16**), inclusions in one rock imply the pregarnet assemblage contained muscovite, clinoamphibole, paragonite, and clinopyroxene, and that garnet nucleated at P-T conditions of ~12.5 kbar and ~475°C (based on QuiG barometry and Zr-in-rutile thermometry, recalculated according to combined calibration of Kohn 2020; Castro & Spear 2017) (**Figure 16**). However, an equilibrium thermodynamic model (**Figure 16*a***), which assumes no surface free energy contribution to garnet, implies garnet nucleated at ~11 kbar and ~600°C, at least 50°C and 5 kbar higher than the predicted garnet isograd (red curve with maximum P-T conditions of ~530°C and 6 kbar, **Figure 16*a***), and far removed from thermobarometric results. An alternate overstepping model (**Figure 16*b***) predicts assemblages in the absence of garnet and then calculates the P-T location of the garnet isograd assuming different amounts of surface free energy (green curves, **Figure 16*b***). A

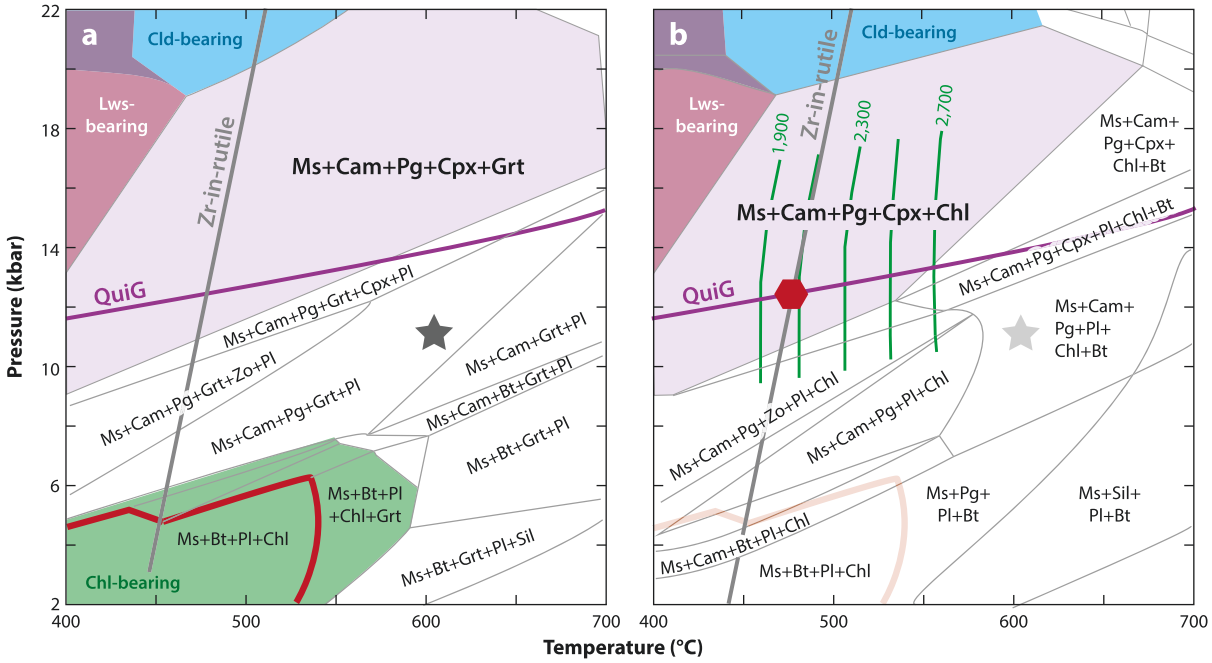

Figure 16

Comparison of equilibrium versus overstepping thermodynamic models for blueschist from Sifnos, Greece. (*a*) Equilibrium thermodynamic model. The star represents the garnet core nucleation condition that would be inferred chemically. This P-T condition differs markedly from the garnet isograd (*red curve*) determined from the whole-rock composition and from intersection of the QuiG barometer and Zr-in-rutile thermometer (recalculated using Kohn 2020, combined calibration). Inferred assemblage prior to garnet growth (*lavender field* of Ms+Cam+Pg+Cpx+Chl) does not overlap star. (*b*) Overstepping thermodynamic model. Green curves represent potential garnet isograds corresponding with different assumed surface free energies from 1,900 to 2,700 J/mol·O. A surface free energy of value of ~2,100 J/mol·O reconciles garnet isograd, inclusion assemblage, QuiG barometry, and Zr-in-rutile thermometry. The gray star and light red curve duplicate the dark gray star and red curve from panel *a* for comparison. Figure adapted from Castro & Spear (2017). Abbreviations: Bt, biotite; Cam, clinoamphibole; Chl, chlorite; Cld, chloritoid; Cpx, clinopyroxene; Grt, garnet; Lws, lawsonite; Ms, muscovite; Pg, paragonite; Pl, plagioclase; QuiG, quartz-in-garnet; Sil, sillimanite; Zo, zoisite; Zr, zirconium.

surface free energy of ~2,100 J/mol·O reconciles the thermodynamic model with thermobarometry (red hexagon, **Figure 16*b***) and inferred pregarnet assemblage (lavender field, **Figure 16*b***) but also implies garnet nucleated far from equilibrium and that its core chemistry cannot be used to infer nucleation conditions or a P-T path. Zhong et al. (2020b) suggested that viscous relaxation might affect QuiG pressures and spuriously imply overstepping. Although theoretically possible, peak temperatures are too low (all less than 600°C; most less than 550°C) for viscous relaxation to be likely for samples considered by Spear et al. (2014) and Castro & Spear (2017). Overall, some studies imply garnet nucleates far from equilibrium (e.g., hexagon versus star in **Figure 16*b***), whereas other studies imply simultaneous chemical and mechanical equilibrium (**Figure 15*b***). The conditions under which equilibrium versus disequilibrium occur remain an area of active research.

Seismic Cycles

Many quartz inclusions in garnet show variation in P_{inc} and P_{trap} that do not distribute regularly with radial position or garnet chemistry (e.g., **Figure 17**). Because viscous or plastic deformation

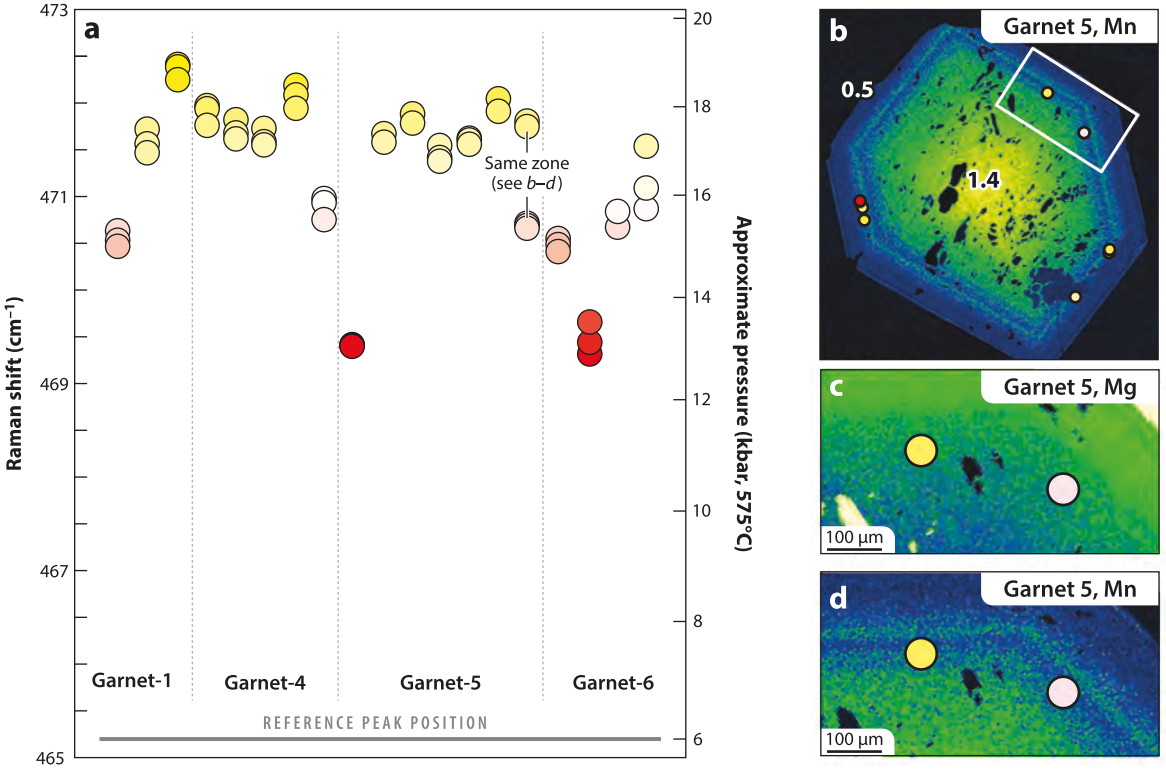

Figure 17

(*a*) Quartz-in-garnet results from blueschist-eclogite block at Ring Mountain, California (Franciscan Formation), showing a range of values that does not simply correlate with location in garnet. Dots are color-coded according to wavelength shift of the A1g peak (nominally ~465 cm^{-1}). Pressures are calculated for quartz-in-almandine (properties from Angel et al. 2017a, 2022b). (*b–d*) Mn and Ca X-ray maps for garnet-5 with high-Mn annulus (*light blue band*). The white box in panel *b* outlines the region in panels *c* and *d* that contains two quartz inclusions with very different wavelength shifts despite indistinguishable garnet chemistry. These variations and oscillations in major element chemistry are interpreted to reflect pressure pulses that dissolve and regrow garnet. Figure adapted from Viete et al. (2018).

can readily release elastic strain, many researchers rely on the maximum P_{trap} value at any radial position to represent P_{trap}. Cracking is not always visible to justify this assumption, however. In contrast, Viete et al. (2018) argued that the variation represents pressure oscillations related to pressure pulses. In their model, fluid-mediated overpressures build up, and then seismic waves trigger release of fluid and pressure. Because garnet typically grows with increasing pressure, these pressure cycles not only produce variation in QuiG pressures but also dissolve and regrow garnets, explaining oscillations in major elements. For example, dissolution should cause a buildup of Mn on garnet rims while regrowth should deplete Mn, resulting in a high-Mn annulus. García-Casco et al. (2002) similarly argued for more than a dozen P-T oscillations, based on compositional oscillations in an eclogitic garnet from the Northern Serpentinite Melange, Cuba. Cyclic variations in pressure might also form in melange zones via repeated formation and release of force chains among interacting blocks, again related to seismic cycles (Beall et al. 2019).

Many other QuiG data sets, measured via Raman spectroscopy, also show nonsystematic variations in P_{inc} and P_{trap} among inclusions, in both subduction and collisional settings (e.g., Spear et al. 2014, Wolfe & Spear 2020, Zhong et al. 2021c, Harvey et al. 2021). Some of this variation might

reflect idiosyncrasies of measurements across inclusions with stress gradients [if they are faceted (**Figure 4**)], but otherwise this observation could imply many garnets in diverse tectonic settings also record seismic cycles. Most garnets do not show major element oscillations, however, so the link between chemistry and elastic thermobarometry is less clear. Compositional oscillations can also form via changes in the rate of P-T increases, rather than via P-T oscillations, if intergranular transport is relatively slow (Kohn 2004). The large pressure drops of several kilobar indicated by QuiG (**Figure 17*a***) imply shear stresses on the order of several kilobars in subduction zones, at least at pressures of 15–20 kbar. Such shear stresses are much higher than typically inferred from rock mechanics (e.g., see Agard et al. 2016) and might help explain why exhumed subducted rocks record higher temperatures than inferred from models that assume little or no shear heating (e.g., Penniston-Dorland et al. 2015, Kohn et al. 2018). Based on pressure differences between QuiG and thermodynamic modeling, Zhong et al. (2021c) also inferred differential stresses up to 10 kbar in eclogitized granulites from the Bergen Arcs, Norway, that are cut by pseudotachylites.

FUTURE RESEARCH

From the most simplified to the most sophisticated models, being able to extend elastic geothermobarometry to more than just a few host-inclusion pairs will require the joint efforts of diverse research communities. A surprisingly major obstacle is the lack of availability of elastic properties at P and T! Even for simple and very common minerals such as quartz, we still do not have reliable measurements of the elastic properties at simultaneous high T and P above 3 kbar. Elastic properties represent the base of any calculation for host-inclusion systems. From simpler X-ray diffraction to more complex and time-consuming Brillouin spectroscopy, data from high P-T experiments are not commonly available and often restricted to high-symmetry crystals. Research on elastic properties has progressively emphasized minerals that form at extreme P-T conditions, overlooking opportunities for substantial development offered by shallower (lower-pressure) materials, such as most of the host-inclusion systems relevant to metamorphic research.

Also surprisingly lacking are calibrations of Raman shifts with pressure. These are of pivotal importance because they provide fundamental insight into the behavior of host-inclusion pairs and for characterizing and interpreting P_{inc}. These experiments are typically performed in diamond anvil cells, which require specialized preparation skills, but are otherwise relatively simple and fast (e.g., a calibration can be performed in less than a month). Yet calibrations are not available for many common mineral inclusions, such as pyrrhotite, ilmenite, hydroxyl-apatite, titanite, amphiboles, and some pyroxenes (e.g., jadeite), let alone more exotic minerals. Simple EoSs have been applied to diverse mineral pairs to predict their thermometric and barometric value (Kohn 2014, Cisneros & Befus 2020), and these predictions could help define future research efforts, especially for minerals with lower symmetry.

Widespread enthusiasm engendered with the recognition that Raman measurements are sufficiently precise for widespread application of QuiG, ZiG, and other elastic thermobarometers (Enami et al. 2007, Endo et al. 2012, Ashley et al. 2014, Kohn 2014, Spear et al. 2014) has been tempered as subsequent research showed how simple elastic models do not always explain the behavior of host-inclusion systems (Campomenosi et al. 2018, 2021; Mazzucchelli et al. 2018, 2019; Murri et al. 2018, 2022; Alvaro et al. 2020; Zhong et al. 2020b, 2021a; Gonzalez et al. 2021). Yet, whereas sophisticated models have now been developed for elastic systems, even more complex models are needed to model inelastic processes. Constraining these models will require more experiments and experimental strategies, both to determine the properties of minerals and to test the fundamental hypotheses behind the models. Computational modeling at different scales (e.g.,

atomistic simulations combined with continuum mechanics) is needed to predict the behavior of minerals under conditions that are difficult to reproduce with experiments. Finally, nature has conducted diverse experiments in the form of exhumed rocks, and these provide opportunity to further test models and develop new concepts. Elastic thermobarometry is an inverse problem with numerous variables. Not all variables are equally important or resolvable, so [the results of Alvaro et al. (2020) notwithstanding] a single inclusion may not provide accurate P-T information if interpreted alone. However, patterns may emerge when numerous inclusions are carefully interpreted together and further help us decipher the evolution of rocks.

DISCLOSURE STATEMENT

The authors are not aware of any affiliations, memberships, funding, or financial holdings that might be perceived as affecting the objectivity of this review.

ACKNOWLEDGMENTS

Thanks to Roberta Rudnick for encouraging this review and for providing comments that helped improve this work. We gratefully acknowledge support from US NSF grants EAR1918488 and OIA1545903 (M.J.K.), a fellowship from the Chinese Academy of Sciences (M.J.K.), an Alexander von Humboldt research fellowship (M.L.M.), and the European Research Council under the Horizon 2020 Research and Innovation Program for the ERC Starting Grant "TrueDepths" N. 714936 (M.A.) and the PRIN-MUR project "THALES" Prot.2020WPMFE9_003. Our understanding of elastic thermobarometry has especially benefited from discussions and collaborations with R. Angel, M. Caddick, N. Campomenosi, E. Moulas, M. Murri, and F. Spear.

LITERATURE CITED

Adams HG, Cohen LH, Rosenfeld JL. 1975. Solid inclusion piezothermometry I: comparison dilatometry. *Am. Mineral.* 60:574–83

Agard P, Yamato P, Soret M, Prigent C, Guillot S, et al. 2016. Plate interface rheological switches during subduction infancy: control on slab penetration and metamorphic sole formation. *Earth Planet. Sci. Lett.* 451:208–20

Alvaro M, Mazzucchelli ML, Angel RJ, Murri M, Campomenosi N, et al. 2020. Fossil subduction recorded by quartz from the coesite stability field. *Geology* 48:24–28

Angel RJ, Allan DR, Miletich R, Finger LW. 1997. The use of quartz as an internal pressure standard in high-pressure crystallography. *J. Appl. Crystallogr.* 30(4):461–66

Angel RJ, Alvaro M, Gonzalez-Platas J. 2014a. EosFit7c and a Fortran module (library) for equation of state calculations. *Zeits. Kristall. Crystall. Matl.* 229(5):405–19

Angel RJ, Alvaro M, Miletich R, Nestola F. 2017a. A simple and generalised *P–T–V* EoS for continuous phase transitions, implemented in EosFit and applied to quartz. *Contrib. Mineral. Petrol.* 172(5):29

Angel RJ, Alvaro M, Nestola F. 2022a. Crystallographic methods for non-destructive characterization of mineral inclusions in diamonds. *Rev. Mineral. Geochem.* 88(1):257–305

Angel RJ, Gilio M, Mazzucchelli M, Alvaro M. 2022b. Garnet EoS: a critical review and synthesis. *Contrib. Mineral. Petrol.* 177(5):54

Angel RJ, Mazzucchelli ML, Alvaro M, Nestola F. 2017b. EosFit-Pinc: a simple GUI for host-inclusion elastic thermobarometry. *Am. Mineral.* 102(9):1957–60

Angel RJ, Mazzucchelli ML, Alvaro M, Nestola F. 2020. "EosFit-Pinc: a simple GUI for host-inclusion elastic thermobarometry"—reply to Zhong et al. *Am. Mineral.* 105(10):1587–88

Angel RJ, Mazzucchelli ML, Alvaro M, Nimis P, Nestola F. 2014b. Geobarometry from host-inclusion systems: the role of elastic relaxation. *Am. Mineral.* 99(10):2146–49

Angel RJ, Mazzucchelli ML, Gonzalez-Platas J, Alvaro M. 2021. A self-consistent approach to describe unit-cell-parameter and volume variations with pressure and temperature. *J. Appl. Cryst.* 54:1621–30

Angel RJ, Murri M, Mihailova B, Alvaro M. 2019. Stress, strain and Raman shifts. *Zeits. Kristall. Crystall. Matl.* 234:129–40

Angel RJ, Nimis P, Mazzucchelli ML, Alvaro M, Nestola F. 2015. How large are departures from lithostatic pressure? Constraints from host–inclusion elasticity. *J. Metamorph. Geol.* 33(8):801–13

Anzolini C, Nestola F, Mazzucchelli ML, Alvaro M, Nimis P, et al. 2019. Depth of diamond formation obtained from single periclase inclusions. *Geology* 47(3):219–22

Ashchepkov IV, Pokhilenko NP, Vladykin NV, Logvinova AM, Afanasiev VP, et al. 2010. Structure and evolution of the lithospheric mantle beneath Siberian craton, thermobarometric study. *Tectonophysics* 485(1–4):17–41

Ashley KT, Caddick MJ, Steele-MacInnis MJ, Bodnar RJ, Dragovic B. 2014. Geothermobarometric history of subduction recorded by quartz inclusions in garnet. *Geochem. Geophys. Geosyst.* 15:350–60

Barron LM. 2003. A simple model for the pressure preservation index of inclusions in diamond. *Am. Mineral.* 88(10):1615–19

Beall A, Fagereng Å, Ellis S. 2019. Fracture and weakening of jammed subduction shear zones, leading to the generation of slow slip events. *Geochem. Geophys. Geosyst.* 20(11):4869–84

Bonazzi M, Tumiati S, Thomas JB, Angel RJ, Alvaro M. 2019. Assessment of the reliability of elastic geobarometry with quartz inclusions. *Lithos* 350–351:105201

Bose K, Ganguly J. 1995. Quartz-coesite transition revisited: reversed experimental determination at 500–1200°C and retrieved thermochemical properties. *Am. Mineral.* 80:231–38

Bower AF. 2010. *Applied Mechanics of Solids*. Boca Raton, FL: CRC

Brewster D. 1820. Notice respecting a singular structure in the diamond. *Edinb. Philos. J.* 3:98–100

Campomenosi N, Angel RJ, Alvaro M, Mihailova B. 2022. Resetting of zircon inclusions in garnet: implications for elastic thermobarometry. *Geology*. In press. **https://doi.org/10.1130/G50431.1**

Campomenosi N, Mazzucchelli ML, Mihailova B, Scambelluri M, Angel RJ, et al. 2018. How geometry and anisotropy affect residual strain in host-inclusion systems: coupling experimental and numerical approaches. *Am. Mineral.* 103(12):2032–35

Campomenosi N, Scambelluri M, Angel RJ, Hermann J, Mazzucchelli ML, et al. 2021. Using the elastic properties of zircon-garnet host-inclusion pairs for thermobarometry of the ultrahigh-pressure Dora-Maira whiteschists: problems and perspectives. *Contrib. Mineral. Petrol.* 176(5):36

Castro AE, Spear FS. 2017. Reaction overstepping and re-evaluation of peak P–T conditions of the blueschist unit Sifnos, Greece: implications for the Cyclades subduction zone. *Int. Geol. Rev.* 59:548–62

Cesare B, Parisatto M, Mancini L, Peruzzo L, Franceschi M, et al. 2021. Mineral inclusions are not immutable: evidence of post-entrapment thermally-induced shape change of quartz in garnet. *Earth Planet. Sci. Lett.* 555:116708

Chopin C. 1984. Coesite and pure pyrope in high-grade blueschists of the Western Alps: a first record and some consequences. *Contrib. Mineral. Petrol.* 86:107–18

Chou I-M, Wang A. 2017. Application of laser Raman micro-analyses to Earth and planetary materials. *J. Asian Earth Sci.* 145:309–33

Cisneros M, Ashley KT, Bodnar RJ. 2020. Evaluation and application of the quartz-inclusions-in-epidote mineral barometer. *Am. Mineral.* 105(8):1140–51

Cisneros M, Befus KS. 2020. Applications and limitations of elastic thermobarometry: insights from elastic modeling of inclusion-host pairs and example case studies. *Geochem. Geophys. Geosyst.* 21(10):e2020GC009231

Cizina MF, Mikesell TD, Kohn MJ. 2023. Optimizing Raman spectral collection for quartz and zircon crystals for elastic thermobarometry. *Am. Mineral.* In press. **https://doi.org/10.2138/am-2022-8423**

Dabrowski M, Powell R, Podladchikov Y. 2015. Viscous relaxation of grain-scale pressure variations. *J. Metamorph. Geol.* 33:859–68

Dubessy J, Caumon M-C, Rull F, eds. 2012. *Raman Spectroscopy Applied to Earth Sciences and Cultural Heritage*. London: Eur. Mineral. Union

Enami M, Nishiyama T, Mouri T. 2007. Laser Raman microspectrometry of metamorphic quartz: a simple method for comparison of metamorphic pressures. *Am. Mineral.* 92(8–9):1303–15

Endo S, Wallis SR, Tsuboi M, Torres De Leon R, Solari LA. 2012. Metamorphic evolution of lawsonite eclogites from the southern Motagua fault zone, Guatemala: insights from phase equilibria and Raman spectroscopy. *J. Metamorph. Geol.* 30(2):143–64

Eshelby J. 1957. The determination of the elastic field of an ellipsoidal inclusion, and related problems. *Proc. R. Soc. A* 241:376–96

Futergendler S, Frank-Kamenetsky V. 1961. Oriented inclusions of olivine, garnet and chrome-spinel in diamonds. *Zap. Vsesoy. Mineral. Obsh.* 90:230–36

Gaidies F, Pattison DRM, de Capitani C. 2011. Toward a quantitative model of metamorphic nucleation and growth. *Contrib. Mineral. Petrol.* 162(5):975–93

García-Casco A, Torres-Roldan RL, Millan G, Monie P, Schneider J. 2002. Oscillatory zoning in eclogitic garnet and amphibole, Northern Serpentinite Melange, Cuba: a record of tectonic instability during subduction? *J. Metamorph. Geol.* 20:581–98

Gilio M, Scambelluri M, Angel RJ, Alvaro M. 2021. The contribution of elastic geothermobarometry to the debate on HP versus UHP metamorphism. *J. Metamorph. Geol.* 40:229–42

Gonzalez JP, Mazzucchelli ML, Angel RJ, Alvaro M. 2021. Elastic geobarometry for anisotropic inclusions in anisotropic host minerals: quartz-in-zircon. *J. Geophys. Res. Solid Earth* 126(6):e2021JB022080

Goodier JN. 1933. Concentration of stress around spherical and cylindrical inclusions and flaws. *J. Appl. Mech.* 55(7):39–44

Guiraud M, Powell R. 2006. *P–V–T* relationships and mineral equilibria in inclusions in minerals. *Earth Planet. Sci. Lett.* 244(3–4):683–94

Guo J, Zheng J, Cawood PA, Weinberg RF, Ping X, Li Y. 2021. Archean trondhjemitic crust at depth in Yangtze Craton: evidence from TTG xenolith in mafic dyke and apatite inclusion pressure in zircon. *Precambrian Res.* 354:106055

Harris JW. 1972. Black material on mineral inclusions and in internal fracture planes in diamond. *Contrib. Mineral. Petrol.* 35:22–33

Harris JW, Milledge HJ, Barron THK, Munn RW. 1970. Thermal expansion of garnets included in diamond. *J. Geophys. Res.* 75(29):5775–92

Harvey KM, Penniston-Dorland SC, Kohn MJ, Piccoli PM. 2021. Assessing *P-T* variability in mélange blocks from the Catalina Schist: Is there differential movement at the subduction interface? *J. Metamorph. Geol.* 39(3):271–95

Holland TJB, Powell R. 2011. An improved and extended internally consistent thermodynamic dataset for phases of petrological interest, involving a new equation of state for solids. *J. Metamorph. Geol.* 29:333–83

Hopkins JB, Farrow LA. 1986. Raman microprobe determination of local crystal orientation. *J. Appl. Phys.* 59:1103–10

Hoskin PWO, Rodgers KA. 1996. Raman spectral shift in the isomorphous series $(Zr_{1-x}Hf_x)SiO_4$. *Eur. J. Solid State Inorg. Chem.* 33:1111–21

Izraeli ES, Harris JW, Navon O. 1999. Raman barometry of diamond formation. *Earth Planet. Sci. Lett.* 173(3):351–60

Knittle E, Williams Q. 1993. High-pressure Raman spectroscopy of $ZrSiO_4$: observation of the zircon to scheelite transition at 300 K. *Am. Mineral.* 78(3–4):245–52

Kohn MJ. 2004. Oscillatory- and sector-zoned garnets record cyclic (?) rapid thrusting in central Nepal. *Geochem. Geophys. Geosyst.* 5:e2004GC000737

Kohn MJ. 2014. "Thermoba-Raman-try": calibration of spectroscopic barometers and thermometers for mineral inclusions. *Earth Planet. Sci. Lett.* 388:187–96

Kohn MJ. 2016. Metamorphic chronology—a tool for all ages: past achievements and future prospects. *Am. Mineral.* 100(1–2):25–42

Kohn MJ. 2020. A refined zirconium-in-rutile thermometer. *Am. Mineral.* 105:963–71

Kohn MJ, Castro AE, Kerswell B, Ranero CR, Spear FS. 2018. Shear heating reconciles thermal models with the metamorphic rock record of subduction. *PNAS* 115:11706–11

Kohn MJ, Spear FS. 1991. Error propagation for barometers: 2. Application to rocks. *Am. Mineral.* 76:138–47

Korsakov AV, Perraki M, Zhukov VP, De Gussem K, Vandenabeele P, Tomilenko AA. 2009. Is quartz a potential indicator of ultrahigh-pressure metamorphism? Laser Raman spectroscopy of quartz inclusions in ultrahigh-pressure garnets. *Eur. J. Mineral.* 21(6):1313–23

Mazzucchelli ML, Angel RJ, Alvaro M. 2021. EntraPT: an online platform for elastic geothermobarometry. *Am. Mineral.* 106(5):830–37

Mazzucchelli ML, Burnley P, Angel RJ, Morganti S, Domeneghetti MCC, et al. 2018. Elastic geothermobarometry: corrections for the geometry of the host-inclusion system. *Geology* 46(3):231–34

Mazzucchelli ML, Reali A, Morganti S, Angel RJ, Alvaro M. 2019. Elastic geobarometry for anisotropic inclusions in cubic hosts. *Lithos* 350–351:105218

Mitchell R, Giardini A. 1953. Oriented olivine inclusions in diamond. *Am. Mineral.* 38:136–38

Morganti S, Mazzucchelli ML, Alvaro M, Reali A. 2020. A numerical application of the Eshelby theory for geobarometry of non-ideal host-inclusion systems. *Meccanica* 55:751–64

Moulas E, Kostopoulos D, Podladchikov Y, Chatzitheodoridis E, Schenker FL, et al. 2020. Calculating pressure with elastic geobarometry: a comparison of different elastic solutions with application to a calc-silicate gneiss from the Rhodope Metamorphic Province. *Lithos* 378–379:105803

Moulas E, Zingerman K, Vershinin A, Levin V, Podladchikov Y. 2021. Large strain formulations for host-inclusion systems and their applications to mineral elastic geobarometry. Paper presented at the EGU General Assembly 2021, online, Apr. 19–30. **https://doi.org/10.5194/egusphere-egu21-14498**

Mura T. 1987. *Micromechanics of Defects in Solids*. Dordrecht, Neth.: Springer

Murri M, Gonzalez JP, Mazzucchelli ML, Prencipe M, Mihailova B, et al. 2022. The role of symmetry-breaking strains on quartz inclusions in anisotropic hosts: implications for Raman elastic geobarometry. *Lithos* 422–423:106716

Murri M, Mazzucchelli ML, Campomenosi N, Korsakov AV, Prencipe M, et al. 2018. Raman elastic geobarometry for anisotropic mineral inclusions. *Am. Mineral.* 103(11):1869–72

Nestola F, Pasqual D, Smyth JR, Novella D, Secco L, et al. 2011. New accurate elastic parameters for the forsterite-fayalite solid solution. *Am. Mineral.* 96(11–12):1742–47

Nimis P, Angel RJ, Alvaro M, Nestola F, Harris JW, et al. 2019. Crystallographic orientations of magnesiochromite inclusions in diamonds: What do they tell us? *Contrib. Mineral. Petrol.* 174(4):29

Nye JF. 1985. *Physical Properties of Crystals: Their Representation by Tensors and Matrices*. Oxford, UK: Oxford Univ. Press. 2nd ed.

Osborne ZR, Thomas JB, Nachlas WO, Baldwin SL, Holycross ME, et al. 2019. An experimentally calibrated thermobarometric solubility model for titanium in coesite (TitaniC). *Contrib. Mineral. Petrol.* 174(4):34

Parkinson CD. 2000. Coesite inclusions and prograde compositional zonation of garnet in whiteschist of the HP-UHPM Kokchetav massif, Kazakhstan: a record of progressive UHP metamorphism. *Lithos* 52(1–4):215–33

Parkinson CD, Katayama I. 1999. Present-day ultrahigh-pressure conditions of coesite inclusion in zircon and garnet: evidence from laser Raman microspectroscopy. *Geology* 27:979–82

Pattison DRM, De Capitani C, Gaidies F. 2011. Petrological consequences of variations in metamorphic reaction affinity. *J. Metamorph. Geol.* 29:953–77

Penniston-Dorland SC, Kohn MJ, Manning CE. 2015. The global range of subduction zone thermal structures from exhumed blueschists and eclogites: Rocks are hotter than models. *Earth Planet. Sci. Lett.* 428:243–54

Pliny the Elder. 1855. *Naturalis Historia*. transl. J Bostock. London: Taylor & Francis. **http://www.perseus.tufts.edu/hopper/text?doc=urn:cts:latinLit:phi0978.phi001.perseus-eng1**

Puhan B. 2021. *Investigation of microscale fracture opening in host inclusion systems*. MS Thesis, Univ. Pavia, Italy

Reher C, Frison G. 1991. Rarity, clarity, symmetry: quartz crystal utilization in hunter-gatherer stone tool assemblages. In *Raw Material Economies Among Prehistoric Hunter-Gatherers*, ed. A Montet-White, S Holen, pp. 375–97. Lawrence: Univ. Kansas

Rosenfeld JL, Chase AB. 1961. Pressure and temperature of crystallization from elastic effects around solid inclusions in minerals? *Am. J. Sci.* 259:519–41

Russell JK, Sparks RSJ, Kavanagh JL. 2019. Kimberlite volcanology: transport, ascent, and eruption. *Elements* 15(6):405–10

Schmidt C, Steele-MacInnis M, Watenphul A, Wilke M. 2013. Calibration of zircon as a Raman spectroscopic pressure sensor to high temperatures and application to water-silicate melt systems. *Am. Mineral.* 98(4):643–50

Schmidt C, Ziemann MA. 2000. In-situ Raman spectroscopy of quartz: a pressure sensor for hydrothermal diamond-anvil cell experiments at elevated temperatures. *Am. Mineral.* 85(11–12):1725–34

Sobolev NV, Fursenko BA, Goryainov SV, Shu JF, Hemley RJ, et al. 2000. Fossilized high pressure from the Earth's deep interior: the coesite-in-diamond barometer. *PNAS* 97:11875–79

Sorby HC, Butler PJ. 1869. On the structure of rubies, sapphires, diamonds, and some other minerals. *Proc. R. Soc.* 17:291–302

Spear FS. 2017. Garnet growth after overstepping. *Chem. Geol.* 466:491–99

Spear FS, Thomas JB, Hallett BW. 2014. Overstepping the garnet isograd: a comparison of QuiG barometry and thermodynamic modeling. *Contrib. Mineral. Petrol.* 168:1059

Stangarone C, Angel R, Prencipe M, Mihailova B, Alvaro M. 2019. New insights into the zircon-reidite phase transition. *Am. Mineral.* 104:830–37

Steno N. 1669. *De Solido Intra Solidum Naturaliter Contento Dissertationis Prodromus*. Florence, Italy: Ex typographia sub signo stellae

Taguchi T, Igami Y, Miyake A, Enami M. 2019. Factors affecting preservation of coesite in ultrahigh-pressure metamorphic rocks: insights from TEM observations of dislocations within kyanite. *J. Metamorph. Geol.* 37:401–14

Tait S. 1992. Selective preservation of melt inclusions in igneous phenocrysts. *Am. Mineral.* 77(1–2):146–55

Thomas JB, Spear FS. 2018. Experimental study of quartz inclusions in garnet at pressures up to 3.0 GPa: evaluating validity of the quartz-in-garnet inclusion elastic thermobarometer. *Contrib. Mineral. Petrol.* 173:42

van der Molen I, van Roermund HLM. 1986. The pressure path of solid inclusions in minerals: the retention of coesite inclusions during uplift. *Lithos* 19(3):317–24

Viete DR, Hacker BR, Allen MB, Seward GGE, Tobin MJ, et al. 2018. Metamorphic records of multiple seismic cycles during subduction. *Sci. Adv.* 4:eaaq0234

Wallis D, Hansen LN, Britton TB, Wilkinson AJ. 2019. High-angular resolution electron backscatter diffraction as a new tool for mapping lattice distortion in geological minerals. *J. Geophys. Res. Solid Earth* 124(7):6337–58

Whitney DL, Broz M, Cook RF. 2007. Hardness, toughness, and modulus of some common metamorphic minerals. *Am. Mineral.* 92:281–88

Whitney DL, Cooke ML, Du Frane SA. 2000. Modeling of radial microcracks at corners of inclusions in garnet using fracture mechanics. *J. Geophys. Res.* 105(B2):2843–53

Wolfe OM, Spear FS. 2020. Regional quartz inclusion barometry and comparison with conventional thermobarometry and intersecting isopleths from the Connecticut Valley Trough, Vermont and Massachusetts, USA. *J. Petrol.* 61(8):3gaa076

Wurz S. 2013. Technological trends in the Middle Stone Age of South Africa between MIS7 and MIS3. *Curr. Anthropol.* 54:S305–19

Zhang Y. 1998. Mechanical and phase equilibria in inclusion-host systems. *Earth Planet. Sci. Lett.* 157(3–4):209–22

Zhong X, Andersen NH, Dabrowski M, Jamtveit B. 2019a. Zircon and quartz inclusions in garnet used for complementary Raman thermobarometry: application to the Holsnøy eclogite, Bergen Arcs, Western Norway. *Contrib. Mineral. Petrol.* 174(6):50

Zhong X, Dabrowski M, Jamtveit B. 2019b. Analytical solution for the stress field in elastic half-space with a spherical pressurized cavity or inclusion containing eigenstrain. *Geophys. J. Int.* 216(2):1100–15

Zhong X, Dabrowski M, Jamtveit B. 2021a. Analytical solution for residual stress and strain preserved in anisotropic inclusion entrapped in an isotropic host. *Solid Earth* 12(4):817–33

Zhong X, Dabrowski M, Powell R, Jamtveit B. 2020a. "EosFit-Pinc: a simple GUI for host-inclusion elastic thermobarometry" by Angel et al. (2017)—discussion. *Am. Mineral.* 105(10):1585–86

Zhong X, Loges A, Roddatis V, John T. 2021b. Measurement of crystallographic orientation of quartz crystal using Raman spectroscopy: application to entrapped inclusions. *Contrib. Mineral. Petrol.* 176(11):89

Zhong X, Moulas E, Tajčmanová L. 2018. Tiny timekeepers witnessing high-rate exhumation processes. *Sci. Rep.* 8(1):2234

Zhong X, Moulas E, Tajčmanová L. 2020b. Post-entrapment modification of residual inclusion pressure and its implications for Raman elastic thermobarometry. *Solid Earth* 11(1):223–40

Zhong X, Petley-Ragan AJ, Incel SHM, Dabrowski M, Andersen NH, Jamtveit B. 2021c. Lower crustal earthquake associated with highly pressurized frictional melts. *Nat. Geosci.* 14:519–25

Zhukov VP, Korsakov AV. 2015. Evolution of host-inclusion systems: a visco-elastic model. *J. Metamorph. Geol.* 33:815–28

Ziman JM. 1960. *Electrons and Phonons: The Theory of Transport Phenomena in Solids*. Oxford, UK: Oxford Univ. Press